ABSTRACT

Title of Dissertation: Ultracold Gases in a Two-Frequency Breathing Lattice

Aftaab Dewan
Doctor of Philosophy, 2024

Dissertation Directed by: Professor Steven L. Rolston
Joint Quantum Institute (JQI)
National Institute of Standards and Technology (NIST)
Department of Physics, University of Maryland

Driven systems have been of particular interest in the field of ultracold atomic gases. The precise control and relative purity allows for construction of many novel Hamiltonians. One such system is the 'breathing' lattice, where both the frequency and amplitude is modulated in time, much like an accordion. We present the results of a phenomenological investigation of a proposed experiment, one where we apply a two-frequency breathing lattice to an atomic system. The results are surprising, as they indicate the possibility of a phase-dependent transition between nearest-neighbour and beyond nearest-neighbour interactions.

Ultracold Gases in a Two-Frequency Breathing Lattice

by

Aftaab Dewan

Dissertation submitted to the Faculty of the Graduate School of the
University of Maryland, College Park in partial fulfillment
of the requirements for the degree of
Doctor of Philosophy
2024

Advisory Committee:
Professor Steve L. Rolston: Advisor, Chair
Professor Ronald L. Walsworth, Dean's Representative
Professor Gretchen K. Campbell
Professor Ki-yong Kim
Professor Nathan Schine

Dedication

To C.B., J.B.F. and R.B.

'the little that we get for free, the little of our earthly trust'

Acknowledgments

No thesis is the product of a singular person. To repeat a cliche, 'it takes a village'. I was lucky in that my 'village' is full of many wonderful people who've supported and cheered me on during this process, and even before that.

My high school physics teacher, Dr. Kumaraswamy, who taught me that free-body diagrams can solve (almost) any problem, and who was my first exposure to what it meant to be a physicist. Radhika Herzberger, who is responsible for the rather large collection of the LRB that I now own.

I'm thankful to the faculty of Physics and Maths departments at Amherst College for encouraging me in my pursuits, and answering my unusual questions with enthusiasm. Jagu, who was always an inspiration, and taught me creativity and Field Theory. David Hall, who emphasised the fundamental nature of uncertainty, and who sparked my interest in Atomic Physics and BECs. Will Loinaz, who's legendary exams often left all of us scratching our heads. Larry Hunter, who introduced my to EEDM, and to the difficulty of measuring zero. Jonathan Friedman, who taught us how to write about experiments, and how to accept our results for what they are. Rob Benedetto, who introduced me to XKCD and who was the reason I almost became a mathematician. David Cox, who let me write the maths comps before I was mat major, and taught me linear algebra. Dan Velleman, who taught me Set Theory and with whom I had many conversations about

interpretations of quantum mechanics. Beyond these departments, I'd like to thank Jeff Ferguson for teaching me how to ask questions, Uday Mehta for ensuring that I learned writing and that I went to Amherst, and Kim Townsend for introducing me to Elizabeth Bishop.

Life has changed a lot since I entered grad school, I lost an appendix, and the world lived through a pandemic. I'd like to thank my advisor, Steve Rolston, for sticking with me the whole way. We've been through a lot, from the lab implosion to switching tracks, and I would not have made it here without him.

I'd like to also thank the whole AMO group at JQI/UMD, who took a bunch of bright eyed grad students and turned them into atomic physicists. Gretchen Campbell and Trey Porto deserve special mention for teaching us atomic physics. I'd also To the group of graduate students I entered with, most of whom have since left for greener pastures; Ana, Andrew, Steve, Gina, Neal, Ken and Dalia: Thank you for making the transition from an undergrad to a grad student pleasant.

Special thanks to Alessandro Restelli, who is single-handedly responsible for raising the quality of electronic projects at JQI by an order of magnitude. Even though very little of what we worked on made it into the thesis, I still learned a lot about PCB design and production, for which I will always be grateful.

When I joined the lab, I was guided along by Matt Reed and Zach Smith. Matt Reed taught me how to run the lab, and how to think about lasers and alignment. I'd also like to thank him for alerting me to the dangers of over-tightening screws, and no Matt, steel is not a liquid. This thesis would have not been possible without Zach Smith. He believed in me, especially when I didn't believe in myself. He made the prospect of running a whole

experiment by myself less daunting, and even after graduating has always been available and willing to answer questions and nudge me in the right direction. He deserves more credit than I can give him. I'd also like to thank Varun Vaidya for being an honorary member of the lab, and being willing to answer questions and talk about things beyond atomic physics.

I'd like to thank all of my incredible friends; Sarah, Alexa, Dana, Tim, Zach and Saugat. Even though we may not see each other as often, knowing that you're always there to talk has been source of strength. I'd like to especially thank my local friends: Rohan, Jenny, Ariel and Conrad (with an honourable mention to Pappe for being the best boy).

You all made living in the area a joy, and gave me a reason to stay for the first time in my life.

None of this would have happened without the support of family. My parents, who've believed in when I most needed it, and have done more for me from halfway across the globe than I would have ever imagined. My brother, who's motivated me my whole life, and especially during grad school.

And finally, I'd like to thank $C_{13}H_{18}CINO$ and C. for keeping me sane.

Table of Contents

Dedication ii

Acknowledgements iii

Table of Contents vi

List of Tables viii

List of Figures ix

List of Abbreviations xi

Chapter 1: Introduction 1
1.1 Distributions and Condensates . . . 1
1.2 The Anatomy of the Thesis . . . 3

Chapter 2: Ultracold physics in dilute atomic gases 4
2.1 Laser Cooling and Mageneto-Optical Traps (MOTs) . . . 4
2.1.1 Lattices . . . 7
2.2 Evaporation . . . 8
2.3 Re-pumpers . . . 9
2.4 Imaging . . . 9

Chapter 3: Conducting experiments using the HiBAL 12
3.1 The Rebuild . . . 12
3.1.1 Zeeman Slower . . . 13
3.1.2 The MOT . . . 13
3.1.3 Moving the Cloud . . . 14
3.1.4 In the Science Cell . . . 14
3.2 The Leak . . . 15

Chapter 4: Overview of Floquet Theory 18
4.1 Introduction . . . 18
4.2 The Theorem . . . 18
4.3 Using Floquet's Theorem to solve the Schrödinger Equation . . . 19
4.3.1 Truncation and Convergence . . . 23

Chapter 5: Breathing Lattices 25
5.1 Motivation . . . 25
5.2 Bloch Functions . . . 26
5.2.1 Sinusoidal Lattice Potential . . . 28
5.3 Breathing Lattices . . . 32
5.3.1 Single Modulation Frequency . . . 32

Chapter 6: Breathing Lattices in two-frequencies 44
6.1 Motivation . . . 44
6.2 The Two-Frequency $k(t)$ . . . 44
6.3 Multi-frequency Floquet theory . . . 45
6.4 Results . . . 52
6.4.1 Γ-dependent tunnelling modification . . . 52
6.4.2 Modifications from R . . . 53
6.4.3 Emergence of divergent behaviour . . . 55
6.4.4 Analysis and possible sources of this phenomena . . . 61
6.5 Experimental plan and potential challenges . . . 62
6.6 Future Work . . . 65

Chapter 7: Conclusion 67

Appendix A: Publication: Griffiths Physics in an Ultracold Bose Gas 68
A.1 Abstract . . . 68
A.2 Introduction . . . 68
A.3 Experimental Approach . . . 70
A.4 Analysis . . . 75
A.5 Conclusion . . . 83

Appendix B: Commutation relations for $\mathcal{D}_\kappa$ and $\mathcal{Y}_\alpha$ 85

Appendix C: Proof of Floquet's Theorem 86

Bibliography 94

List of Tables

6.1 Range over which behaviour like fig. 6.8 was observed. 57

List of Figures

3.1 The MOT coil with epoxy applied to the two leak locations 17

5.1 Band structure schematic, where $\delta \propto V_r$ 30
5.2 Plot taken from [1], showing agreement between the simulation (the orange and purple dots), and $\mathcal{J}_0$ (the orange line) 41

6.1 Nearest neighbour tunnelling amplitude as a function of site index for three different Γ value for $m = 2, n = 3$. (a) shows the tunnelling for $\gamma_1 = .05$ $\gamma_2 = .005$. (b) shows the tunnelling for $\gamma_1 = .05$ $\gamma_2 = .045$, and (c) is for $\gamma_1 = .02$, $\gamma_2 = .07$ 53
6.2 Tunnelling plot for $m = 3, n = 4$ 54
6.3 Tunnelling plot for $m = 3, n = 5$ 54
6.4 Γ scan for $m = 2, n = 3$ 55
6.5 Γ scan for $m = 1, n = 2$ 55
6.6 Γ scan for $m = 1, n = 3$ 56
6.7 Plot contrasting the effective Hamiltonian of $\Gamma < 1$ with $\Gamma \approx 1$, showing the couplings between the different lattice sites. For both $\Gamma < 1$ and $\Gamma \approx 1$, we only have nearest neighbour coupling. And they show the $\mathcal{J}_0$ tunnelling exhibited by $\Gamma < 1$, and the deviation from it for $\Gamma \approx 1$. It is important to note that the deviation occurs towards the edges of the lattice, leaving the center relatively unperturbed 57
6.8 Tunnelling plot for $m = 2, n = 3$ at $\gamma_1 = .12$ and $\gamma_2 = .2$ 58
6.9 Effective Hamiltonian for fig. 6.8 58
6.10 Plot showing the onset of higher-order couplings 59
6.11 Progression of divergent tunnelling, characterised by $\vartheta = \frac{J(0)-\mathcal{J}_0(0)}{|\min(J(0))-\mathcal{J}_0(0)|}$ . . 60

A.1 A diagram of the superfluid pancakes in the generated disordered layered optical potential 72
A.2 An example image from the experiment, along with its $n_\perp$ and $n_\parallel$ distributions 74
A.3 The fraction of atoms in the Thomas-Fermi distribution as a function of temperature 75
A.4 A random sampling of images at a few temperature ranges in our 2.8 kHz lattice 77
A.5 The average density profile for the coldest temperatures together with $\overline{n}_\perp$. 77

A.6 The mean fluctuation correlations of the momentum $\overline{\alpha}(p_a, p_b, T)$ 78
A.7 Normalized $p, -p$ correlations β 79
A.8 Squared fluctuations $\overline{\alpha}(p, p)$ 82

List of Abbreviations

1D	one dimension
2D	two dimension
3D	three dimension
AOM	acousto-optic modulator
BEC	Bose-Einstein condensate
BKT	Berezinskii-Kosterlitz-Thouless
JQI	Joint Quantum Institute
MOT	Magneto-Optical trap
RF	Radio Frequency
TDSE	Time dependent Schrödinger Equation
TISE	Time Independent Schrödinger Equation
TOF	Time of flight
FBZ	First Fourier-Brillouin Zone

Chapter 1: Introduction

Since their prediction [2], and creation in a cold atom setting[3] [4], Bose-Einstein Condensates have become an ubiquitous tool in modern physics. Their pristine nature, and the fine control available make them at attractive option for task ranging from sensors[5], clocks[6] or even simulating more exotic systems like gravitational waves [7].

1.1 Distributions and Condensates

Bose-Einstein condensation is a phenomena unique to bosons[1]. It occurs because bosons don't obey the Pauli Exclusion principle, and hence multiple bosons can be in the same quantum state. A condensate forms when a non-negligible fraction of the total atom number is in the ground state, and they collectively act a macroscopic quantum object.

For a group of bosons, we can write the single particle occupation number for the energy state i using Bose Statistics

$$\tilde{n}_i = \frac{1}{e^{\beta(\epsilon_i - \mu)} - 1}. \tag{1.1}$$

Here ϵ_i is the energy of state i. μ is the chemical potential, and $\beta = \frac{1}{k_B T}$[2]. For a

[1] Nature is endlessly creative, so condensation can even occur when fermions group up to imitate bosonic behaviour. As is the case in BCS superconductivity[8]

[2] At high temperatures or low particle number, both Fermi-Dirac and Bose statistics reduce to the usual

dilute gas in 3D the transition to BEC occurs when the phase space density [3]

$$D = n\left(\frac{2\pi\hbar}{mk_bT}\right)^{3/2} \tag{1.2}$$

is of order 1[4](where n is the number density). This gives us the transition temperature T_c,

$$T_c = \frac{2\pi}{k_b}\frac{\hbar^2 n^{2/3}}{\zeta(3/2)^{2/3}m} \tag{1.3}$$

below which atoms begins to collect in the ground state. The proportion of atoms in the excited state is given by

$$N_{ex} = N\left(\frac{T}{T_c}\right)^{\alpha} \tag{1.4}$$

where N is total particle number and α is related the system's density of states[5]. This in turn lets us compute the condensate fraction, which is the number of atoms in the BEC as

$$N_0 = N\left[1 - \left(\frac{T}{T_c}\right)^{\alpha}\right]. \tag{1.5}$$

We'd like to note the importance of α here, because while $\alpha = \frac{3}{2}$ for a free particle in a 3D box, in a 3D harmonic trap $\alpha = 3$; Since $\frac{T}{T_c} < 1$, this implies that condensation is easier in harmonic traps, which also explains their ubiquity in BEC experiments.

Maxwell-Boltzmann statistics

[3]A good derivation of these results can be found in [9]

[4]More precisely, $D \geq \zeta(3/2) \approx 2.6$

[5]This is because for a large number of commonly encountered system, the density of states is $g(\epsilon) \propto \epsilon^{\alpha-1}$

1.2 The Anatomy of the Thesis

I would like to comment on the somewhat unusual nature of the thesis. We began this project with the goal of using our lab setup (described briefly in Chapter 3) to generate a 1D breathing lattice,

$$V_{br} = \left(\frac{k(t)}{k_0}\right)^2 V_0 \cos(k(t)x) \tag{1.6}$$

where $k(t) \propto 1 + \gamma \cos(\Omega_{br} t)$. Our goal was to subject our BEC to this potential, and then observe the effect it had on the properties of the cloud. And since breathing lattices themselves had not been used as the object of study, we were quite excited by the prospect.

However, the pandemic threw a wrench into our plans, and we had to unfortunately close the lab. As a result, we had to change our focus. This is reflected in the thesis, where we go over the progress we had made towards conducting the experiment, before switching to a more theoretical analysis of the breathing lattice extended to two-frequencies.

Chapter 2: Ultracold physics in dilute atomic gases

As mentioned in the introduction, our experiment ended up becoming a casualty of COVID-19. As such, the experiment as it was no longer exists or functions. Nonetheless, it is still fruitful to understand the principles and techniques that go behind conducting experiment in ultra cold atomic gases.

2.1 Laser Cooling and Mageneto-Optical Traps (MOTs)

The fundamental technique that makes any of this possible is the usage of lasers to manipulate atoms. This includes cooling, trapping, and the generation of optical lattices. These techniques are well understood and ubiquitous in modern atomic physics [10] [11][12].

The principle behind laser cooling combines momentum conservation with the Doppler Effect. When an atom moving in a direction collides with a counter-propagating photon that it's resonant with, it absorbs the photon and enters an excited state. This is combined with a momentum kick in the direction of the photon's travel. Symmetry considerations then require that the photon be emitted in a random direction, which then imparts a momentum kick in a random direction. Repeated over many such events, this can be averaged to a force exerted on the atoms

$$F_s = \hbar k \frac{\Gamma}{2} \frac{I/I_{sat}}{1 + I/I_{sat} + 4(\delta - \mathbf{k} \cdot \mathbf{v})^2/\Gamma^2}. \tag{2.1}$$

$\hbar k$ is the photon's momentum, Γ is the spontaneous decay rate of the atom and I_{sat} is the saturation intensity for this particular transition. I is the intensity of the laser beam, and δ is the laser's detuning from resonance. The $\mathbf{k} \cdot \mathbf{v}$($\mathbf{k}$ is the wave-vector of the laser and $\mathbf{v}$ is atomic velocity) term is the shift in detuning due to the Doppler effect. As the atomic velocity changes, the 'effective' detuning does as well. This continues until the force exerted becomes small enough to have a negligible effect on the atom's momentum. We can now imagine using six such beams, two along each axis, which damps the total momentum, and cools the atoms. This has a lower bound, known as the Doppler cooling limit [13], as fluctuations and spontaneous emissions limit the average kinetic energy of the atoms. This state is sometimes referred to as an 'optical molasses' [14], and the lower bound on its temperature is

$$T_{doppler} = \frac{\hbar \Gamma}{2k_b}. \tag{2.2}$$

Even before going further, one can notice that this is not sufficient to trap the atoms. An atom with a temperature $\approx T_{doppler}$ can slowly wander outside the region where the beams intersect and then it is no longer subject to the radiation pressure. What we would like is a spatially dependent δ to confine the atoms.

One way to accomplish this is using the Zeeman effect. A magnetic field with a zero at this intersection can be used to provide a restoring force. This is called a MOT[15][16] , or a Magneto-Optical Trap. A commonly used configuration(and the one we used in our lab) is to use a quadrupole trap to provide a field gradient in all directions, and then to

detune the lasers from resonance at the field zero. We choose the polarisations of each beam pair to be σ^+ and σ^-, so that they address states with opposing magnetic moments. The net effect of this is that as atoms move away from the centre, one of the beams shifts towards resonance, and the other away from resonance. This imbalance in the scattering rates has the effect of providing a force toward the centre, where the de-tunings are the same[1]. This principle is also applied in the construction of a Zeeman slower [19], which is used to cool the atoms initially to a temperature where they can be captured by the MOT.

One technique we have not mentioned so far is the usage of far off-resonant light for trapping[20]. The electric field E of a laser beam induces an electric dipole moment $p \propto E$ in atom. This dipole then interacts with the field, generating a potential $V_{dip} \propto pE$. Since the intensity of the beam $I \propto E^2$, and using $F_{dip} = \nabla V_{dip}$, we have

$$V_{dip} \propto E^2 \tag{2.3}$$

$$\propto I \tag{2.4}$$

$$F_{dip} \propto \nabla I. \tag{2.5}$$

The sign of this potential depends on the sign of the detuning, with red-detuned light generating an attractive potential, while blue-detuned light generates a repulsive one. This allows to create purely optical traps using high-intensity red-detuned lasers. An additional

[1]It is possible to trap atoms solely using a magnetic field [17], but 'Majorana' flips around the field zero causes the trap to leak and lose atoms[18]. Which in turn can be mitigated by using a Time-orbiting potential (TOP)[3] trap, but we leave that discussion for elsewhere.

advantage is that for a typical beam with a Gaussian profile,

$$I \propto I_0 e^{\frac{-x^2}{w_0^2}}, \tag{2.6}$$

the potential experienced by our atoms is essentially harmonic near the centre of the focused beam.

2.1.1 Lattices

We can also imagine using this dipole force to generate a lattice potential for the atoms. A pair of counter propagating beams will form a standing wave, which generates alternating peaks and troughs. The lattice potential in this case is

$$V_l(x) = V_0 \cos^2(k_l x) = V_0/2\,(1 + 2\cos(2k_l x)) \tag{2.7}$$

$k_l = 2\pi/\lambda$ is the wave-vector for light of wavelength λ. We should note that the beams need not be counter-propagating, even beams at a shallow angle (θ) will generate a lattice with spacing

$$d = \frac{\lambda}{2\sin(\theta/2)}. \tag{2.8}$$

$\theta = \pi$ reduces to $d = \lambda/2$ for the counter-propagating lattice, and $\theta = 0$ gives $d = \infty$, which is what one would expect from parallel beams. A shallow angle lattice has an additional travelling component transverse to the lattice[2], but is identical in behaviour otherwise. As we can see, by varying V_0 and k_l, we can even create a stack of very narrow pancakes, which

[2]For large de-tunings, this travelling component applies very little radiation pressure, and can be safely neglected

allows us to create quasi-2D periodic potentials.

This technique can be extended to generate a whole range of potentials, in both 2D and 3D, limited only by our control over the beam geometry, making it a very powerful tool.

2.2 Evaporation

It turns out that the Doppler temperature is typically not low enough to allow for condensation, so we require further cooling. An easy technique to accomplish this is Polarisation gradient cooling [21, 22]. If we have two counter-propagating laser beams with orthogonal linear polarisations, they generate a polarisation standing wave along the direction of propagation. The gradient from this wave provides a damping force which further cools the atoms using the Sisyphus effect [11]. In our lab this is implemented by having linearly polarised MOT beams, which are then retro-reflected. This allows one to reach much lower temperatures than with just Doppler cooling.

The final step in the cooling process is evaporation, which removes higher-energy atoms from the trap, hence lowering the mean energy of the remaining cloud [23]. As mentioned earlier, an optical dipole trap provides an ideal method to accomplish this, as the intensity is easily controlled[23],[24] , [25], [26]. For atoms in magnetic trap, this can be done by using RF. The RF is used as a 'knife' to shave the edge of magnetic trap. This ejects the higher energy atoms[27]. The RF is used to flip the spin of these atoms, which makes the field anti-trapping. Since these atoms are closer to the edge, they have higher energies, and removing them lowers the mean energy of the remaining atoms.

Either of these techniques provides sufficient cooling to form a BEC.

2.3 Re-pumpers

In actual experiments, the complex atomic structure necessitates the usage of additional beams to keep the atoms in states which are resonant with the main trapping beams. For instance, in our experiment we use the D_2 line for ^{87}Rb. The particular transition we use is from $^2S_{1/2}$ to $^2P_{3/2}$ at 780.241 nm. The ground state for this transition has $F = 1$ and $F = 2$ manifolds separated by 6.8 GHz, and the excited state has $F = 0$ to $F = 3$ manifolds. We use the state $F = 1$, $m_F = -1$. (This data has been compiled by [28])

If the atoms decay back down to a different state, they are then 'dark' to our main trapping beams, and would consequently fall out of the trap. To prevent this, we use additional re-pumper beams which send these states back to the appropriate excited state. Since the two ground band manifolds are separated by 6.8 GHz, the re-pumpers are tuned 6.8GHz away from the main MOT beam. This keeps our atoms in the main trapping cycle, and plugs any leaks we might have.

2.4 Imaging

Having created the BEC, the best method of data collection is imaging. Which can either be non-destructive[29] [30], or destructive. We use absorption imaging, using the atomic cloud's shadow to infer the spatial distributions, which is a destructive measurement.

To compute these distributions, we need the optical scattering cross-section σ. This

is a purely a function of the transition,

$$\sigma_0 = \frac{\hbar\omega\Gamma}{2I_{sat}} \tag{2.9}$$

and if the light is off resonance or at a higher intensity

$$\sigma = \frac{\sigma_0}{1 + 4\left(\frac{\delta}{\Gamma}\right)^2 + \frac{I}{I_{sat}}} \tag{2.10}$$

Once we have our image, and using the optical depth τ of the medium, we can use Beer's[31] law to relate the final intensity to the initial intensity,

$$I = I_0 e^{-\tau} = I_0 e^{-n\sigma}. \tag{2.11}$$

Using this, we can compute density n of the cloud from a picture, assuming we have I and I_0.

For out experiment, we take three pictures for every sample. The first image is taken with the cloud present, let us call this F_a. The second picture is taken immediately after the atoms leave the frame, which gives us our probe beam, let's call this F_p. The final image is a 'dark' image, with neither the probe or the atoms present (F_d), this lets us correct for any background not from the probe or the atoms[3]. If these images are taken close enough together in time, we can reasonably assume that the probe intensity is the same for the first two pictures.

The CCD readout is in counts/pixel, and to convert from there to the intensity

[3]This is typically to correct for CCD specific patterns

requires one to consider various aspects of the imaging system. This includes magnification, the quantum efficiency of the camera, the gain from the conversion electronics, the size of the CCD and the duration of the pulse. These can be all combined in a conversion coefficient β to convert from count/pixel to intensity/count. Luckily, to first approximation the optical depth is

$$\tau = \ln\left(\frac{F_p - F_d}{F_a - F_d}\right) \tag{2.12}$$

Where the factor of β cancels out. Using eq. (2.11) and this, we can get the column density of the cloud. We can combine this with other physical properties of the system like trap frequency, time-of-flight etc.. to reconstruct the cloud and its physical properties.

Chapter 3: Conducting experiments using the HiBAL

As mentioned in the introduction, our lab became a casualty of COVID-19, and such it is no longer in working order. But before that occurred, we developed the HiBAL[1], and used it to observe the sliding phase[32]. This work was done by Matt Reed, Zach Smith and myself, and the resulting publication is presented as Appendix A.

In this chapter, we will briefly discuss what made our lab suited to conducting the breathing lattice experiment, and what would be probably required for others to conduct this experiment. Both Zach Smith [1] and Matt Reed [33] have gone over the details of running and construction in extensive detail, so we will limit our discussion to the more unique features of our apparatus.

3.1 The Rebuild

When I joined the lab, it was mid-way through a rebuild of our main apparatus responsible for creating ^{87}Rb BECs. The reasons behind this were twofold, firstly we wanted to modernise our lab to reduce time spent optimising, and increase time spent conducting experiments. Secondly, we wanted greater optical access to our BEC cloud, to give us the ability to subject the cloud to complex optical potentials.

[1] High-Bandwith Arbitrary Lattice

We accomplished this by designing our experiment such that after condensation our atoms were in the 'Science Cell', which is a rectangular quartz cell measuring $1.25 \times 2.25 \times 4.5$ cm with 1.25 mm thick walls. On the open end, it was attached via a glass-to-metal seal to the main MOT chamber. This gave us optical access from five of the six sides. Getting the atoms there, however, was not an easy feat.

3.1.1 Zeeman Slower

Our atoms start out as a hot gas of ^{87}Rb atoms at 400 K coming out from our oven. This gas is then collimated by an aperture into the Zeeman slower, which is a long tube with a carefully tuned spatially dependent magnetic field gradient, which when combined with beam travelling through it, slows our atoms down enough to be captured by our MOT.

3.1.2 The MOT

Our MOT design was one that had been used in the JQI before, so we were confident of its reliability[34]. It consisted of a quadrupole magnetic field generated by a water cooled coil, and two separate lasers to address the main and repumping transitions respectively.

Once we have a large enough cloud of atoms in the MOT, we transfer them to a magnetic trap for RF evaporation. We do this because the next step involves transferring the atoms to a dipole trap, and for that we need the cloud to be small enough to match the dipole trap's cross-section. Our dipole trap was provided by a 15W 1550 nm laser with waist of $\approx 60\mu m$ at its focus. Once the cloud is cold enough, we ramp on the dipole trap, and ramp off the magnetic trap.

3.1.3 Moving the Cloud

After the atoms have been transferred to the dipole beam, they are still in the main MOT chamber. To move them to the Science cell, we used a an air-bearing stage[2] to smoothly move the focus of the dipole beam by 30 cm out to the cell [35]. The acceleration profile must be carefully chosen to minimise loss, but once that is done, this method is remarkably stable at transferring atoms from the MOT chamber to the science cell[3].

3.1.4 In the Science Cell

Once the cloud has been successfully moved, we can use the full capabilities of our HiBAL to manipulate it. Our HiBAL was able to generate a wide range of phase-stabilised optical lattices. The main lattice beams were generated by a titanium-sapphire laser with a wavelength near 780 nm. The phase-locking was accomplished by a piezo mirror along one of the beam paths, which was servo'd by a signal from an interferometer custom built to allow phase locking of multiple different frequencies at the same time. All of this was possible because we were able to procure a custom wide-bandwidth AOM from IntraAction. The different frequencies from the AOM would serve as Fourier components, which we would pulse on adiabatic timescales to generate the desired potential at the atoms. This analogue signal came from an arbitrary-waveform generator (AWG), which was pre-programmed with the correct pulse train.

It was this capability to generate and phase-stabilise lattices that made us confident in

[2] Aerotech ABL20040-10

[3] There can be additional interference from stray RF or magnetic fields, but a track of rare earth magnets along the travel path solves this problem [33]

our ability to generate the breathing lattice. We would use a DDS (direct digital synthesis) system to generate pulse-train for our AWGs, which would then feed into the AOM.

3.2 The Leak

As anyone who has worked in an experimental setting is well aware, keeping an experiment functional is a constant battle against entropy. Under ordinary circumstances, the daily operation of the lab keeps this entropy low, and things operational. The pandemic changed all that. Quarantining meant leaving the lab unattended for months.

Over one of those quarantine periods, we faced a nightmare scenario. Over a weekend, we got an email from the facilities department at the university that there was a flood outside our lab. When we went in an checked, we discovered that our MOT coil had developed a leak. Since our MOT required 100 A of current for its field, the coil had to be water cooled. We had accomplished this by using a rectangular hollow copper tube for the coil, which could then be hooked up to the lab water supply via a pump to maintain flow.

The coil rested right above our main MOT chamber, and had to be very carefully engineered to provide a clean quadrupole field. The coil and leak can be seen in fig. 3.1, where we have applied epoxy to seal the leak locations.

This fix worked for a time, but it did not last. A few months after, the leak returned, and at this point it seemed unlikely that epoxy would be sufficient to fix it. Rebuilding the coil would take a long time, since it would have to be redesigned and machined from scratch, made harder by the fact that I was the only person running the lab at this point of time. This is not to mention the fairly significant issue that one of our lasers had developed

as well.

So, with a heavy heart, we decided that the best course of action would be to shut down the lab. And I switched my focus from conducting the breathing lattice experiment to seeing if extending it to two-frequencies could be interesting from a theoretical perspective.

The rest of this thesis will discuss that work, and the somewhat surprising results we obtained in doing that simulation.

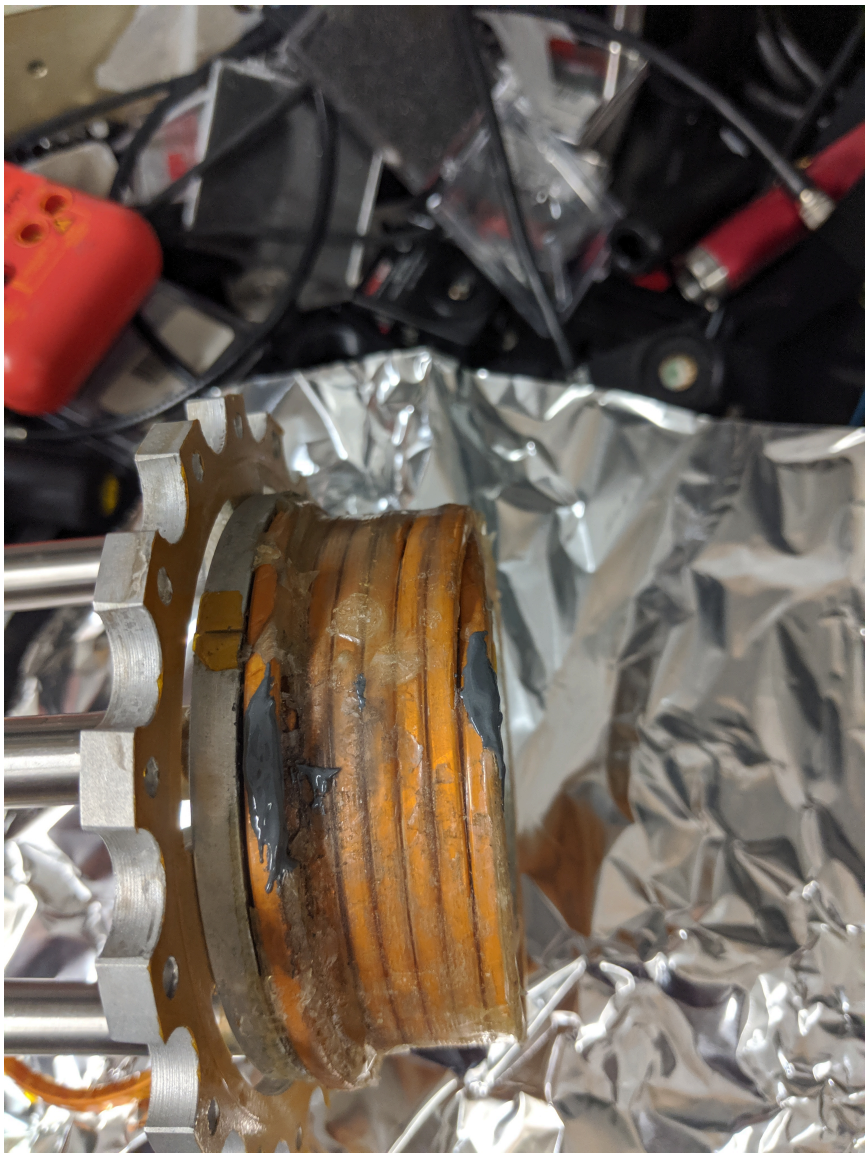

Figure 3.1: The MOT coil with epoxy applied to the two leak locations

Chapter 4: Overview of Floquet Theory

Before we can get to breathing lattices, we need to understand how to treat time-periodic Hamiltonians. This is where Floquet's theorem and it's application to quantum mechanics comes in. We will briefly discuss those in this chapter.

4.1 Introduction

While the usage of Floquet methods is common in modern day physics[36] [37], it's roots predate quantum mechanics. The theorem itself was first proved in 1883 by French mathematician Achille Marie Gaston Floquet[38]. At the time it was a mathematical curiosity, investigating the properties of differential equations with periodic conditions. It was only when combined with Bloch's work[39] that it's applications to physics became clear.

4.2 The Theorem

Floquet's theorem[1] states that for all solutions $\mathbf{x}$ of the differential equation

$$\mathbf{x}' = \mathbf{A}(t)\mathbf{x} \tag{4.1}$$

[1] A proof of this can be found in Appendix C

where $\mathbf{A}(t)$ is periodic with a period T, the following are true:

1. $\mathbf{x}$ may not necessarily be periodic, but it must be of the form $e^{\mu t}\mathbf{p}(t)$, where $\mathbf{p}(t)$ is T periodic.

2. There exist n such μ_j, and they satisfy the condition:

$$e^{\mu_1 T}e^{\mu_2 T}\cdots e^{\mu_n T} = \exp\left(\int_0^T \operatorname{tr}\mathbf{A}(q)dq\right) \tag{4.2}$$

4.3 Using Floquet's Theorem to solve the Schrödinger Equation

Let us now see how we can use this to solve the Time-dependent Schrödinger Equation(TDSE)[2],

$$i\hbar\frac{\mathrm{d}}{\mathrm{d}t}\left|\Psi(t)\right\rangle = H(t)\left|\Psi(t)\right\rangle \tag{4.3}$$

where

$$H(t+T) = H(t) \tag{4.4}$$

Of course, we could write down the stroboscopic time-evolution operator $U(T)$,

$$U(T) = \mathcal{T}\exp\left(-\frac{i}{\hbar}\int_0^T H(t')dt'\right) \tag{4.5}$$

($\mathcal{T}$ denotes time ordering). We can then brute force integrate $U(T)$ and then diagonalise it to obtain Floquet states.

Rather, we will follow Shirley [39] and use Floquet's theorem to transform this into

[2]This section is based on [40] [41]

matrix equation of an Hermitian operator over an extended Hilbert space.

Using Floquet's Theorem , we can write down the solutions to the Schrödinger Equation as:

$$|\psi_n(t)\rangle = e^{-i\epsilon_n t/\hbar} |\Phi_n(t)\rangle \tag{4.6}$$

Where, $|\Phi_n(t)\rangle = |\Phi_n(t+T)\rangle$. ϵ_n is the Floquet 'quasi-energy' of state $|\psi_n(t)\rangle$. Now since the driving hamiltonian is also T periodic, we can write the Φ_n as a discrete Fourier series in the drive frequency $\omega = 2\pi/T$.

$$|\Phi_n(t)\rangle = \sum_m e^{-im\omega t} |\phi_n^{(m)}(t)\rangle \tag{4.7}$$

Here, $\phi_n^{(m)}$ is the m-th Fourier coefficient of $\Phi_n(t)$. However, we must note that in general, these coefficients need not be normalised or orthogonal. The only condition on these coefficients is that they sum to produce the orthogonal Floquet states $|\psi_n(t)\rangle$ for all time t.

Now, our problem has reduced to finding the set of $\{\phi_n^{(m)}\}$ that solve the Schrödinger equation. First, we substitute Eq. 4.6 into Eq. 4.3,

$$\left[\epsilon_n + i\hbar\frac{\mathrm{d}}{\mathrm{d}t}\right] |\Phi_n(t)\rangle = H(t) |\Phi_n(t)\rangle \tag{4.8}$$

Here we have cancelled the phase factor $e^{-i\epsilon_n t/\hbar}$ from both sides. Using the Fourier representations of both $|\Phi_n(t)\rangle$ and $H(t)$, and after some algebra we obtain:

$$(\epsilon_n + m\hbar\omega) |\phi_n^{(m)}\rangle = \sum_{m'} H^{(m-m')} |\phi_n^{(m')}\rangle \tag{4.9}$$

Where, as with $|\phi_n(t)\rangle$, $H^{(m-m')}$ is the $(m-m')$ Fourier coefficient of the hamiltonian H

Now, we can write Eq. 4.9 as an eigenvalue problem in this Fourier space. We write an infinite dimensional column vector φ_n that contains all the Fourier coefficients $|\phi_n^{(m)}\rangle$ as its components. We then rearrange the coefficients in Eq. 4.9 as a matrix $\mathcal{H}$ which acts on the vectors in this Fourier space.

That is,

$$\mathcal{H}\varphi_n = \epsilon_n \varphi_n, \tag{4.10}$$

$$\mathcal{H} = \begin{pmatrix} \ddots & H^{(-1)} & H^{(-2)} & \\ H^{(1)} & H_0 - m\hbar\omega & H^{(-1)} & H^{(-2)} \\ H^{(2)} & H^{(1)} & H_0 - (m+1)\hbar\omega & H^{(-1)} \\ & H^{(2)} & H^{(1)} & \ddots \end{pmatrix}, \tag{4.11}$$

$$\varphi_n = \begin{pmatrix} \vdots \\ |\phi_n^{(m)}\rangle \\ |\phi_n^{(m+1)}\rangle \\ \vdots \end{pmatrix} \tag{4.12}$$

The matrix in Eq. 4.11 is composed of an infinite number of $d \times d$ blocks, where d is the dimension of H. H_0 is the time-averaged (or DC) component of the hamiltonian, $H_0 = \frac{1}{T}\int_0^T H(t)dt$.

As we mentioned, the solutions to Eq. 4.10 belong to the larger Fourier space, which is infinite dimensional. Given that our original system only had dimension d, these solutions must correspond to a set of linearly-dependent quantum states. Moreover, d physical states

must be encoded an infinite number of times in the eigenvectors of $\mathcal{H}$[3]. To see this more clearly, let us consider the Floquet state $|\psi_n(t)\rangle$. We know that

$$|\psi_n(t)\rangle = e^{-i\epsilon_n t/\hbar} \sum_m e^{-im\omega t} |\phi_n^{(m)}\rangle \,. \tag{4.13}$$

This follows from Eq. 4.6 and Eq. 4.7. From here, we can see that we can shift the Floquet-quasi-energy ϵ_n in integer multiples of $\hbar\omega$ without changing the underlying physical state $|\psi_n(t)\rangle$.

$$\begin{aligned} |\psi_n(t)\rangle &= e^{-i(\epsilon_n + m'\hbar\omega)t/\hbar} \sum_m e^{-i(m-m')\omega t} |\phi_n^{(m)}\rangle \\ &\equiv e^{-i\tilde{\epsilon}_n t/\hbar} \sum_m e^{-im\omega t} |\tilde{\phi}_n^{(m)}\rangle \,, \end{aligned} \tag{4.14}$$

Here, we define $\tilde{\epsilon}_n = \epsilon_n + m\hbar\omega$ and $|\tilde{\phi}_n^{(m)}\rangle = |\phi_n^{(m+m')}\rangle$. So, all distinct Floquet state solutions to the Schrödinger Equation fall within an quasi-energy band of width $\hbar\omega$, i.e. $\epsilon_{min} \leq \epsilon < \epsilon_{min} + \hbar\omega$. In an analogy to Bloch's theorem, this is sometimes called the first 'Floquet-Brillouin' zone[42]. A solution outside this zone must correspond to a solution inside the zone whose quasi energy has been shifted by an integer multiple of $\hbar\omega$.

Physically, this behaviour arises from the discrete time-translation symmetry of the system. The Floquet states are stroboscopic eigenstates of the time-translation operator $U(T)$. Since U is unitary, its eigenvalues must be of the form $e^{-i\theta_n}$. By write θ_n as $\epsilon_n T/\hbar$, we introduce the aforementioned degeneracy. This property expresses the fact that in a periodically driven system, the energy is conserved up-to an integer number of photon

[3]This also follows from definition C.0.2

emission or absorption events, each with an energy $\hbar\omega$.

4.3.1 Truncation and Convergence

Having said all that, there is still one problem that remains. If we want to numerically compute these solutions, we will naturally have to truncate our infinite dimensional Fourier space. The question then arises, how large must this truncated space be? Can we obtain approximate solutions that are both accurate and efficient to compute? To find the answers to these questions, let us consider the simple case of a single harmonic drive,

$$H(t) = H_0 + V(t), \quad V(t) = Ve^{i\omega t} + V^\dagger e^{-i\omega t} \tag{4.15}$$

For this system, we can see that $H^{(-1)} = V$, $H^{(1)} = V^\dagger$, and $H^{(\Delta m)} = 0$ for $|\Delta m| > 0$. Now, $\mathcal{H}$ for this system can be written as the tri-diagonal block

$$\mathcal{H} = \begin{pmatrix} \ddots & V & 0 \\ V^\dagger & H_0 - m\hbar\omega & V \\ 0 & V^\dagger & \ddots \end{pmatrix} \tag{4.16}$$

repeated along the diagonal with the time averaged term H_0 shifted by integer multiples of $\hbar\omega$. This very much reminds us of a tight-binding lattice with nearest-neighbour hopping and a linear potential. Taking this further, consider a situation where the system described by H_0 is finite, i.e. has a finite-dimensional Hilbert space. If we ignore the $-m\hbar\omega$ terms, we can think of $\mathcal{H}$ as the hamiltonian of a 'particle' hopping between 'sites' of a one-dimensional lattice in the Fourier harmonic space. H_0 governs the on-site energy and

intra-unit-cell hopping, and V governs the inter-cell-hopping. If H_0 has the dimension one, the kinetic energy of this particle lies within the band $\mathcal{W} = 2|V|$. And, if the dimension is larger than one but still finite, the width of this band still lies between $||V||$ and $||H_0||$ (spaced out in integer multiples of $\hbar\omega$).

If we ignore the $-m\hbar\omega$ terms for a moment, the eigenstates of $\mathcal{H}$ are Bloch waves in this Fourier harmonic space. These states then 'localise' when the $-m\hbar\omega$ terms are introduced in this Fourier space,as one can view the $-m\hbar\omega$ terms here as analogous to potential energy terms. Semi-classically, this means that the 'particle' only ever access harmonics with a band $\mathcal{L}_m \approx \mathcal{W}/(\hbar\omega)$, with the wavefunction decaying rapidly outside this region.

This suggests we should truncate our space to a size $(2M+1)$ where $(2M+1) \gg \mathcal{L}_m$, to ensure reasonable convergence. It is important to note that, as in any truncation, states that are close to the edge will likely be distorted and un-physical. But, as long we follow our guideline, the first Floquet-Brillouin zone solutions will be free from any such pathologies.

Chapter 5: Breathing Lattices

5.1 Motivation

One way to view breathing lattices eq. (1.6) is as analogous to shaken lattices. For atoms in an optical lattice, either a shallow-angle or not, we can think of the shaken lattice as a modulation of the phase of the standing wave. Similarly, a breathing lattice can be thought of as a modulation of the frequency of the same[1].

Shaken lattices have been the subject of extensive investigation, from uses as varied as Quantum Simulation, and as a clean environment for studying driven systems[43, 44, 45, 46, 47, 48]. Breathing lattices have received less attention[49, 50, 51, 52], largely stemming from the fact that they are much harder to generate. A shaken lattice can be generated by position modulation of the retro-reflect mirror (using a piezo for example), but generating a breathing lattice requires either modulating the angle between the beams of the shallow angle lattice, or direct modulation of the laser frequency. The latter was going to be our approach, with a high bandwidth acousto-optic modulator(AOM), and precise control of the AOM driving frequency using our AWGs.

Numerical work investigating the single-frequency case was done by Zach Smith ([1]).

[1]We additionally modulate the amplitude, but that is to ensure that the lattice depth in terms of recoil energies stays constant. This isolates the effect of breathing from modifications to tunnelling from amplitude modulation.

I have extended this to breathing in two different frequencies, and found that there are 'islands' of interesting behaviour that differ sharply from expectations.

5.2 Bloch Functions

In chapter 4, we discussed how to apply Floquet Theorem to a general T periodic Hamiltonian, and transformed the TDSE into an (albeit infinite dimensional) matrix diagonalisation problem. The system we are interested in is an optical lattice that is then subjected to a T periodic modulation. To understand this, let us briefly discuss spatially periodic potentials first. Instead of the standard approach, we will use Floquet's theorem to solve this problem.[2]

Given a spatially periodic Hamiltonian,

$$H(x) = H(x + a) \tag{5.1}$$

where a is the period, we would like to solve the Time-Independent Schrödinger equation for this Hamiltonian,

$$\hat{H} \left|\Psi\right\rangle = E \left|\Psi\right\rangle . \tag{5.2}$$

Restricting ourselves to one dimension, we can write this as

$$\left(\frac{-\hbar^2}{2m}\frac{\mathrm{d}^2}{\mathrm{d}x^2} + V(x)\right)\psi(x) = E\psi(x). \tag{5.3}$$

[2] A more standard discussion of the topics covered in this section can be found in [53, 54]

All the spatial dependence now resides in $V(x)$, (with the requirement that $V(x) = V(x+a)$). If we can transform this second order differential equation to one in first-order, we could apply Floquet's theorem to immediately write down the solutions. Let us define

$$\hat{\varphi}(x) = \begin{pmatrix} \psi(x) \\ \psi'(x) \end{pmatrix} \tag{5.4}$$

and,

$$\mathbf{K}(x) = \begin{pmatrix} 0 & 1 \\ \frac{2m}{\hbar^2}(V(x) - E) & 0 \end{pmatrix}. \tag{5.5}$$

By definition $\mathbf{K}(x) = \mathbf{K}(x+a)$. Now we can re-write the Scrödinger equation as:

$$\hat{\varphi}'(x) = \mathbf{K}(x)\hat{\varphi}(x). \tag{5.6}$$

This form is familiar to us, and it lets us use the results of chapter 4 to write down the solution(in 1D),

$$\psi(x) = e^{ikx}u_k(x) \tag{5.7}$$

where $u_k(x) = u_k(x+a)$. These solutions are called Bloch Functions, after Felix Bloch, who first proved this result [55]. k (sometimes also called q) is the quasi-momentum corresponding to the Bloch Wave. As with Floquet states, these are not unique, as we can write

$$\psi(x) = e^{ikx}u_k(x) = e^{i(k+n(2k_a))x}u_{k+n(2k_a)}(x) \tag{5.8}$$

For $k_a = \pi/a$ (n is any integer). To reduce this degeneracy, we can restrict ourselves to (very much like the Floquet case) a quasi-momentum band of width $2\pi/a$, i.e. $-\pi/a \leq k \leq \pi/a$. This region forms the first 'Brillouin Zone'. We can index the solutions with higher quasi-momentum with n, sometimes called the band index.

5.2.1 Sinusoidal Lattice Potential

Now let us look at the specific case of sinusoidal lattice potential. Consider

$$V(x) = \frac{V_0}{2}\cos(2k_a x) \tag{5.9}$$

Where as before $k_a = \pi/a$. We would now like to solve the Schrödinger equation for the resulting one-dimensional Hamiltonian:

$$H_l = \left(-\frac{\hbar^2}{2m}\frac{\partial^2}{\partial x^2} + V(x)\right). \tag{5.10}$$

One way of accomplishing that is to us plane waves, $e^{i(k+2nk_a)x}$, as our basis set. Which gives us,

$$H_l e^{i(k+2nk_a)x} = \left(-\frac{\hbar^2}{2m}\frac{\partial^2}{\partial x^2} + \frac{V_0}{2}\cos(2k_a x)\right) e^{i(k+2nk_a)x} \tag{5.11}$$

$$= \left(\frac{\hbar^2}{2m}(k+2nk_a)^2 + \frac{V_0}{4}(e^{i2k_a x} + e^{-i2k_a x})\right) e^{i(k+2nk_a)x} \tag{5.12}$$

$$= \frac{\hbar^2}{2m}(k+2nk_a)^2 e^{i(k+2nk_a)x} + \frac{V_0}{4}(e^{i(k+2(n+1)k_a)x} + e^{i(k+2(n-1)k_a)x}) \tag{5.13}$$

This reveals two important features of this Hamiltonian,

1. It couples plane waves that differ by multiples of $2k_a$

2. It also tells us the natural energy scale that governs the problem

$$E_r = \frac{\hbar^2 k_a^2}{2m}, \tag{5.14}$$

This is called the lattice recoil energy, as it is the energy gained from absorbing one unit of lattice momentum.

We can then solve the resulting Schrödinger equation by writing it as a matrix equation,

$$\begin{pmatrix} \ddots & & & & \\ & (\frac{k}{k_a}+2)^2 & V_r/4 & 0 & \\ & V_r/4 & (\frac{k}{k_a})^2 & V_r/4 & \\ & 0 & V_r/4 & (\frac{k}{k_a}-2)^2 & \\ & & & & \ddots \end{pmatrix} \begin{pmatrix} \vdots \\ c_{n,1} \\ c_{n,0} \\ c_{n,1} \\ \vdots \end{pmatrix} = \epsilon_n \begin{pmatrix} \vdots \\ c_{n,1} \\ c_{n,0} \\ c_{n,1} \\ \vdots \end{pmatrix} \tag{5.15}$$

where $\epsilon_n = \frac{E_n}{E_r}$, $V_r = \frac{V_0}{E_r}$,and E_n is the eigenvalue of the state $\psi_{n,k}$[3]. Using the $c_{n,j}$, we can write this state in the plane wave basis as

$$\psi_{n,k} = \sum_j c_{n,j} e^{i(k+2jk_a)x} \tag{5.16}$$

As we mentioned, n is the band index. Setting $n = 0$ restricts us to the first Brillouin Zone.

[3]Each (n, k) denotes a different eigenstate i.e. $\langle \psi_{n,k} | \, | \psi_{n',k'} \rangle \propto \delta_{n,n'} \delta_{k,k'}$)

These solutions can be numerically computed to arbitrary accuracy by adding more tri-diagonal blocks to the matrix. They were also computed exactly by Mathieu when he was investigating vibrations on a drumhead [56], which gave him the same second order differential equation as the one we obtained for the case of a sinusoidal lattice. As such, they are the Mathieu Functions, and they are well understood mathematically.

If we plot the solutions for this problem, we can obtain a physical understanding of the V_r. For $V_r = 0$ we obtain the free particle solution, since there is no binding potential. As we increase V_r, we can see that 'gaps' begin to open up. These gaps are between 'bands' of allowed energies, and they are indexed by n. That is, $\psi_{n,k}$ is the state in the nth band with quasi-momentum k.

Figure 5.1: Band structure schematic, where $\delta \propto V_r$

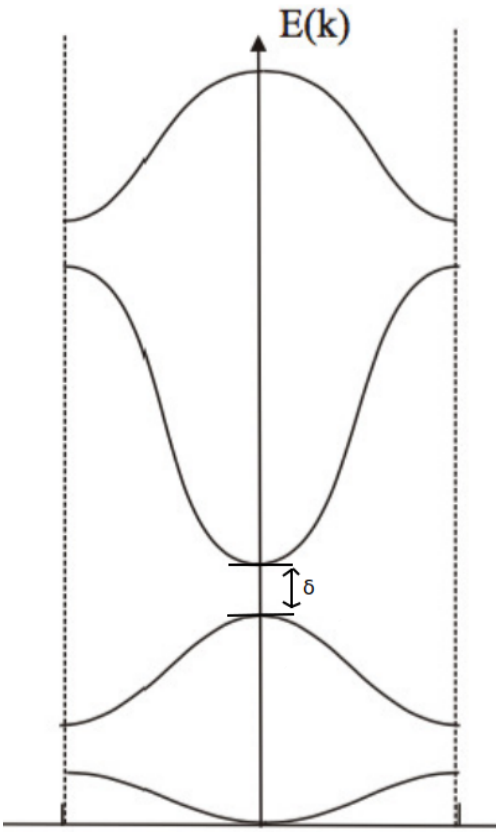

The Bloch wave functions ($\psi_{n,k}$) as written above are delocalised over the whole lattice, but there is another representation which using a basis of localised states. [57] showed that if we have a complete set of Bloch Functions, we can generate a set of Wannier functions using

$$w_n(x - x_j) = \int_{FBZ} u_{n,k} e^{-ikx_j} dk, \tag{5.17}$$

Where we integrate over the first Brillouin zone. Furthermore, it is possible to choose the $u_{n,k}$ phases such that the Wannier Functions obtained are real and decay exponentially outside the site j. The Wannier Functions, like the Bloch Functions, form a complete orthogonal set.

Tight Binding Approximation

Using either of the above representations, it is possible to re-write the Hamiltonian in terms of creation and annihilation operators. For example, in the Wannier basis,

$$\mathcal{H}_l = -\sum_{n,i,j} J_{i,j} a^\dagger_{n,i} a_{n,j}. \tag{5.18}$$

J is the coupling between sites i and j. Since the Wannier functions form a complete orthogonal set, there are no couplings between different bands.

For the situations we will be discussing, we will restrict ourselves to the tight-binding approximation[58]. This approximation is valid when we are dealing with low temperatures and low atom numbers. The low temperature ensures that no atoms are in the higher

bands, and the low atom number allows us to ignore inter-atomic interactions. Both these conditions combined mean that we don't expect any couplings beyond the nearest neighbour. So, our lattice Hamiltonian is now

$$\mathcal{H}_B = -J \sum_{|i-j|=1} a_i^\dagger a_j \tag{5.19}$$

with J as the tunnelling amplitude between adjacent sites.

5.3 Breathing Lattices

Now let us turn to the breathing lattice. For cold atoms we can write the single particle Hamiltonian as

$$H_{br} = \frac{p^2}{2m} + \left(\frac{k(t)}{k_0}\right)^2 V_0 \cos(k(t)x) \tag{5.20}$$

Where the $k(t)$ is periodic in some T, and V_0 is the lattice depth.

5.3.1 Single Modulation Frequency

For a single modulation frequency, we take $k(t)$ as

$$k(t) = k_0 \left(1 + \gamma \cos(\Omega t)\right). \tag{5.21}$$

Here k_0 is the mean k-vector, γ is the amplitude ($\gamma < 1$) and Ω is the frequency of modulation(or the drive). The amplitude term $(k(t)/k_0)^2$ is there to ensure that our lattice

depth in terms of E_r remains constant. This ensures that any behaviour observe can be attributed to the breathing, and not an amplitude modulation.

As noted, this work was done by Zach Smith [1] as part of his thesis. We will present a brief summary of that work, as we will need that background before looking at the two-frequency breathing lattice.

The Hamiltonian in Eq. 5.20 is not trivial. To make the problem tractable, [1] introduced a 'co-breathing' frame with the help of two unitary transformations, a dilation operator $\mathcal{D}_\kappa$

$$\mathcal{D}_\kappa = \exp\left(\frac{i}{\hbar}\log(\kappa)\,\frac{xp+px}{2}\right), \tag{5.22}$$

(where κ is a time-dependent scale factor), and a position dependent momentum shift operator $\mathcal{Y}_\alpha$

$$\mathcal{Y}_\alpha = \exp\left(-\frac{i}{\hbar}\alpha\frac{x^2}{2}\right) \tag{5.23}$$

(where as before α is a time-dependent scale factor).

We also need to know how a Hamiltonian transforms under a time-dependent unitary operator $\mathrm{U_t}$. To do this, let's take the TDSE

$$i\hbar\frac{d}{dt}\left|\Psi\right\rangle = H\left|\Psi\right\rangle \tag{5.24}$$

and apply U_t to both sides,

$$\mathrm{U_t}\, i\hbar\frac{d}{dt}\left|\Psi\right\rangle = \mathrm{U_t}\, H\left|\Psi\right\rangle$$

then, inserting $U_t^\dagger U_t$ and applying the chain rule we obtain

$$i\hbar\left(\frac{d}{dt}(\mathrm{U_t}\,|\Psi\rangle) - \frac{d\,\mathrm{U_t}}{dt}\,|\Psi\rangle\right) = \mathrm{U_t}\,H\,\mathrm{U_t}^\dagger\,\mathrm{U_t}\,|\Psi\rangle \tag{5.25}$$

Which can be re-arranged to obtain

$$i\hbar\frac{d}{dt}\,\mathrm{U_t}\,|\Psi\rangle = (\mathrm{U_t}\,H\,\mathrm{U_t}^\dagger + i\hbar\dot{\mathrm{U}}_\mathrm{t}\,\mathrm{U_t}^\dagger)(\mathrm{U_t}\,|\Psi\rangle) \tag{5.26}$$

which is simply the TDSE again, but for

$$H' = (\mathrm{U_t}\,H\,\mathrm{U_t}^\dagger + i\hbar\dot{\mathrm{U}}_\mathrm{t}\,\mathrm{U_t}^\dagger) \tag{5.27}$$

$$|\Psi\rangle' = \mathrm{U_t}\,|\Psi\rangle \tag{5.28}$$

Now, going back and applying the dilation operator $\mathcal{D}_\kappa$ to Eq. 5.20, we obtain

$$H_\mathcal{D} = \frac{p^2}{2m\kappa^2} + \left(\frac{k(t)}{k_0}\right)^2 V_0\cos(k(t)\kappa x) - \frac{\dot\kappa}{\kappa}\frac{xp+px}{2} \tag{5.29}$$

we can combine the first and third terms to complete the square to obtain

$$H_\mathcal{D} = \frac{(p - m\dot\kappa\kappa x)^2}{2m\kappa^2} + \left(\frac{k(t)}{k_0}\right)^2 V_0\cos(k(t)\kappa x) - \frac{m\dot\kappa^2 x^2}{2} \tag{5.30}$$

Now, we apply the position dependent momentum shift operator $\mathcal{Y}_\alpha$ to obtain

$$H_{\mathcal{Y},\mathcal{D}} = \frac{p^2}{2m\kappa^2} + \left(\frac{k(t)}{k_0}\right)^2 V_o\cos(\kappa(t)x) + \frac{m\kappa\ddot\kappa x^2}{2} \tag{5.31}$$

where have taken $\alpha = m\dot{\kappa}\kappa$. [4] We choose $\kappa = \frac{k_0\sqrt{1+\gamma^2/2}}{k(t)}$ to obtain the final transformed Hamiltonian

$$H' = \frac{1}{\kappa^2}\left(\frac{p^2}{2m} + V_\gamma \cos(k_e x)\right) + \frac{m\kappa\ddot{\kappa}x^2}{2} \tag{5.32}$$

where

$$V_\gamma = (1+\gamma^2/2)V_0 \qquad k_e = \sqrt{1+\frac{\gamma^2}{2}}k_0 \tag{5.33}$$

This form looks more tractable, since we have gathered all the t-dependence in κ and its derivatives. However, it can be shown that the time averaged term is always negative, which gives us anti-trapping potential, and leaves us with no bound Floquet states.[5] In our experiment, however, we use an additional harmonic confining potential with a frequency ω. We can add this to the our Hamiltonian, and apply the same unitary operator transformations to obtain

$$H_f = \frac{1}{\kappa^2}\left(\frac{p^2}{2m} + V_\gamma \cos(k_e x)\right) + \frac{mx^2}{2}(\omega^2\kappa^2 + \kappa\ddot{\kappa}) \tag{5.34}$$

The added harmonic terms provide the additional confinement needed to obtain bound states.

Critical Drive Limit

With the added harmonic term, we now have another parameter we change to influence the Hamiltonian's behaviour. As mentioned, we of course require a κ (which come from

[4] The commutation relations needed to justify the above results are in appendix B

[5] This follows from the fact that κ is an even function, so it can be written with a Fourier series of real coefficients.

our choice of Ω) so that the time-averaged potential does not become negative, but beyond that we are free to pick our constraint. A possible direction is one where we fix our drive frequency such that the time-averaged potential is zero. This has the added benefit of making the numerics much easier to perform. For the case of single frequency, this 'critical' drive is easy to compute, and we obtain:

$$\Omega_c = \frac{\sqrt{2(1-\gamma^2)}}{\gamma}\omega \tag{5.35}$$

This leaves us with γ as the parameter to vary in our simulations. We should that any drive frequency Ω below Ω_c will produce harmonic bound states, but to simplify the computations, we will restrict ourselves to critical drives. For our purposes, we assume that the tight-binding model continues to hold.

5.3.1.1 Numerics and filtering

We will now give some details about our simulation. Since a lot of these techniques will remain the same when we switch to the two-frequency breathing lattice, these will be presented in some detail. Fortunately, we have already done much of the preliminary work in our previous chapter, and we just need to apply those results here. Choosing to work in the Wannier basis, we can write

$$H_0 = -J\sum_j (a_j^\dagger a_{j+1} + a_{j+1}^\dagger a_j) + \mathcal{E} j^2 n_j^2 \tag{5.36}$$

$$\mathcal{E} = \frac{2m\pi^2}{k_e}(\omega^2\kappa^2 + \kappa\ddot{\kappa})^{(0)} \tag{5.37}$$

Where we have used the kinetic energy and the sinusoidal lattice terms to compute J, and used the external harmonic trap as the on-site energy term $\mathcal{E}$[6]. We then compute the higher order Fourier components, and use those to construct our matrix equation eq. (4.10). This can then be solved numerically, as it just a diagonalization problem. $\mathcal{L}_m$ can be estimated from our simulation parameters, to let us decide where to truncate the matrix $\mathcal{H}$.

Filtering

As our criterion for picking $\mathcal{L}_m$ was to ensure that the states in the FBZ converged, any states outside this region are not guaranteed to be physical . So we would like a way to filter out these states. A reasonable requirement is that an atom in the lattice must remain there over the duration of a drive cycle. That means the Floquet state $\psi(t)$, defined in Eq. 4.13, must satisfy

$$\sum_j |\langle j|\psi(t)\rangle|^2 = 1 \tag{5.38}$$

where j sums over the lattice sites. Since states close to edge of Fourier space are unable to interact with up to half of the states one would physically expect, they have a difficult time satisfying this requirement. To filter these out, let us define ρ as

$$\rho = \sum_j |\langle j|\psi(t)\rangle|^2 \tag{5.39}$$

,and the error ϵ as

$$\epsilon = 1 - \rho \tag{5.40}$$

[6] n_j is the number operator at site j, and $^{(0)}$ represents the time-average

Then we can consider the root-mean-square value ϵ_{rms} of this quantity, averaged over the same drive cycle.

$$\epsilon_{rms} = \sqrt{\frac{1}{T}\int_T \epsilon^2 dt} \tag{5.41}$$

So we need to evaluate the integral

$$\frac{1}{T}\int_T 1 - 2\rho + \rho^2 dt \tag{5.42}$$

using the definition of ψ,

$$\rho = \sum_j |\langle n|\psi(t)\rangle|^2 \tag{5.43}$$

$$= \sum_j \left(c^*_{j,m'} e^{-im'\Omega t}\right)\left(c_{j,m} e^{im\Omega t}\right) \tag{5.44}$$

$$= \sum_j \sum_{m,m'} c^*_{j,m'} c_{j,m} e^{i(m-m')\Omega t} \tag{5.45}$$

$$\tag{5.46}$$

which implies,

$$\frac{1}{T}\int_T \rho dt = \frac{1}{T}\int_T \sum_j \sum_{m,m'} c^*_{j,m'} c_{j,m} e^{i(m-m')\Omega t} dt \tag{5.47}$$

$$= \sum_{j,m,m'} c^*_{j,m} c_{j,m'} \delta_{mm'} \tag{5.48}$$

$$= \sum_{j,m} c^*_{j,m} c_{j,m} = 1 \tag{5.49}$$

By definition of ψ. (5.50)

Now,

$$\frac{1}{T}\int_T \rho^2 dt = \frac{1}{T}\int_T \left(\sum_{j,m,m'} c^*_{j,m'} c_{j,m} e^{i(m-m')\Omega t}\right)\left(\sum_{k,n,n'} c^*_{k,n'} c_{k,n} e^{i(n-n')\Omega t}\right) dt \tag{5.51}$$

Looking closely at this, we notice that only the terms where $(m-m') = -(n-n')$ survive,

$$= \sum_{j,m,m',k,n,n'} c^*_{j,m} c_{j,m'} c^*_{k,n} c_{k,n'} \tag{5.52}$$

$$\text{Let } \alpha = m - m' \tag{5.53}$$

$$= \sum_{j,m,\alpha,k,n} c^*_{j,m-\alpha} c_{j,m} c^*_{k,n+\alpha} c_{k,n} \tag{5.54}$$

$$\text{for } \alpha = 0 \tag{5.55}$$

$$\sum_{j,m,k,n} c^*_{j,m} c_{j,m} c^*_{k,n} c_{k,n} = 1 \tag{5.56}$$

$$\tag{5.57}$$

Putting all of the above together, we obtain

$$\frac{1}{T}\int_T \epsilon^2 dt = \sum_{\alpha\neq 0} c^*_{j,m-\alpha} c_{j,m} c^*_{k,n+\alpha} c_{k,n} \tag{5.58}$$

Thinking of the $c_{j,n}$ as a vector we can write,

$$\epsilon_{rms} = \sqrt{\sum_{m,n,\alpha} \left[c^\dagger c\right]_{m-\alpha,m} \left[c^\dagger c\right]_{n+\alpha,n}} \tag{5.59}$$

where we have converted the sums over j,k into the matrix $\left[c^\dagger c\right]$. This form is easily

computable numerically, since $c_{j,m}$ is what we obtain from solving our matrix equation. Eq. 5.59 has a lower bound of 10^{-8} from errors in floating-point arithmetic, but has the advantage of being fast. To give us a higher accuracy in filtering, we first use Eq. 5.59 as a rough filter (for example, $\epsilon_{rms} < 10^{-7}$), then take the remaining states and perform direct numeric integration to compute ϵ_{rms}. This further pushes our errors down to $\approx 10^{-16}$. The simulation is written in Python3[59], making extensive use of the packages SciPy[60],NumPy[61], and mpmath[62]. PyPlot[63] is used to generate the plots.

The first Fourier-Brillouin Zone

Let us call the set of states we obtain after filtering Φ. We now want to find the set of states φ in Φ that comprise the first Fourier-Brillouin zone (FBZ). As we showed in [section on Floquet theory], each distinct physical state ψ will have up-to $2M+1$ occurrences (each shifted by $\hbar\omega$) in Φ. We can use this to group these states, and these groups will then each be a distinct physical state ψ. Let ξ be the set of all quasi energies of Φ, we then construct the set

$$Q_d = \{\, q \mod \hbar\omega \mid q \in \xi \,\} \tag{5.60}$$

We then sort Q_d in ascending order of q_n To group these states, we find the spots where the energy difference between adjacent states ($\delta_n = q_n - q_{n+1}$) is greater than some threshold(ϵ) which is determined by the energy scale of our problem($\propto f(E_r, V_0, \Omega)$) i.e. $|\delta_n| > |\epsilon|$. The states that lie between these spot we can say with reasonable confidence are the same physical state ψ. Since we are in the Wannier basis, if our lattice has j sites, we expect to find j distinct states. In the case of single-frequency breathing, with no inter-band

couplings, this is what our simulations give us. In the other cases, i.e. either multi-frequency breathing or non-zero inter-band couplings, this condition is not always necessarily met. We will discuss what to do in those scenarios later.

Bessel $\mathcal{J}_0$ tunnelling

The central result from the single-frequency simulations is that it gives rise to a site-dependent tunnelling amplitude in the shape of a Bessel $\mathcal{J}_0$. This can be understood as the averaged result of the position dependent shaking experienced by the atoms. [1] gives a derivation for this our system to find the tunnelling amplitude

$$\mathrm{T}(j) = \mathcal{J}_0\left(\frac{\pi\sqrt{2(1-\gamma^2)(1+\gamma^2/2)}}{4}\frac{\hbar\omega}{E_r}j\right), \tag{5.61}$$

and plotted the results, which are shown in fig. 5.2

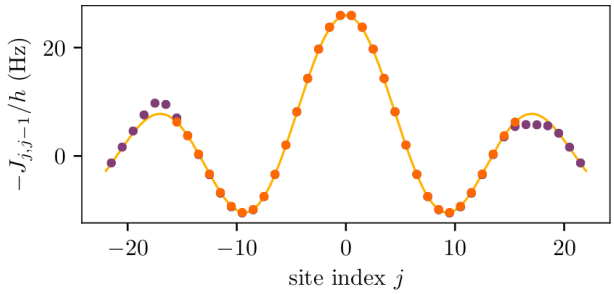

Figure 5.2: Plot taken from [1], showing agreement between the simulation (the orange and purple dots), and $\mathcal{J}_0$ (the orange line)

This is another reason why shaken lattices provide a good analogy, as $\mathcal{J}_0$ tunnelling is also a feature in those systems [47]. Having summarised previous work, we now turn our attention to extending the system to two-frequencies.

Validity of the single band approximation

Before we discuss the two frequency lattice, let us briefly investigate the single-band assumption. If we add inter-band couplings to the Hamiltonian, does that have any effect on the results? To consider a smaller lattice, but we include the states in both the ground band and the first excited band. We then compute the inter-band couplings, and run the simulation using these new off-diagonal terms.

First, let us consider just the lattice part of the 1D Hamiltonian

$$H_0 = \frac{p^2}{2m} + V_0 \cos(k_e x). \tag{5.62}$$

We can solve the Schrödinger equation for this Hamiltonian

$$H_0 \varphi_{n,k}(x) = \varepsilon_{n,k} \varphi_{n,k} \tag{5.63}$$

to obtain the Bloch Waves $\varphi_{n,k}$:

$$\varphi_{n,k}(x) = e^{ikx} u_{n,k} \tag{5.64}$$

Here n is the band index and $u_{n,k}$ periodic.

Now we use these to construct the Wannier functions centred at site j,

$$w_n(x - x_j) = \int_{BZ} e^{-ikx_j} \varphi_{n,k}(x) dk \tag{5.65}$$

x_j is the location of site j. As before, if we are careful with picking our phases, we can ensure that the Wannier functions are real and exponentially localised around x_j. This forms our basis set for band n, and over all j that comprise our lattice. Using these states and the Hamiltonian H, we can compute the matrix elements for the Hamiltonian including the inter-band terms

$$\langle m, i| H |n, j\rangle = \int_{-\infty}^{\infty} w_m^*(x - x_i) \left(H_0 + Ax^2\right) w_n(x - x_j) dx \tag{5.66}$$

Where,

$$A = \frac{m}{2}(\omega^2\kappa^2 + \kappa\ddot{\kappa})^{(0)}. \tag{5.67}$$

From this point, we consider a system with $2j$ sites, with j sites being in each of the ground band and the excited band. We then construct the Hamiltonian for this system, and then use that as the Hamiltonian for our Floquet simulation.

We did simulation of a $2j = 46$ site system, over a wide range of γ values. We found that even if we artificially increased the interband coupling beyond what one would expect, there were no modifications to the $\mathcal{J}_0$ tunnelling behaviour. As such, we concluded that our system lies well within the tight-binding regime, and that we can ignore effects from the presence of higher bands.

Chapter 6: Breathing Lattices in two-frequencies

6.1 Motivation

The main focus of this work was investigating the effects of adding a second modulation frequency to the breathing. We were motivated to explore this direction by considering the behaviour of two-period static lattices, which can be described by using Aubrey-André models [64]. The behaviour of these systems depends on the nature $\beta = \frac{k_2}{k_1}$, the ratio between the two wave-numbers k_1,k_2. For systems with an irrational (or increasingly incommensurate) value of β, the system exhibits a localisation phase transition. This has been observed in both atoms[65] and light[66]. We wanted to see if there was similar behaviour when considering the ratio of the breathing frequencies.

6.2 The Two-Frequency $k(t)$

The form we chose for our two-frequency $k(t)$, in our hamiltonian

$$H_{br} = \frac{p^2}{2m} + \frac{k(t)}{k_0}^2 V_0 \cos(k(t)x) \tag{6.1}$$

is

$$k(t) = k_0(1 + \gamma_1 \cos\Omega_1 t + \gamma_2 \cos\Omega_2 t). \tag{6.2}$$

Where as before $\gamma_1, \gamma_2 < 1$. While this is hard to solve exactly, we can intuit the behaviour by looking at the ratios $\Gamma = \frac{\gamma 1}{\gamma 2}$, and $R = \frac{\Omega_1}{\Omega_2}$. For either both $\Gamma \ll 1$ and $\Gamma \gg 1$ we expect our results to resemble the single frequency scenario, as one of the terms will dominate the breathing behaviour. We expect to see the biggest deviations when $\Gamma \approx 1$. It is less clear what effect varying R would have on the system, as the same limiting scenarios ($R \gg 1$ and $R \ll 1$)do not easily compare to the single frequency case.

6.3 Multi-frequency Floquet theory

Before we proceed further, we need to extend Floquet theory to multiple frequencies. A naive approach could be to take our earlier results and simply add additional Fourier spaces for the new frequencies. Let us see how that would work in the case of two-frequencies. Let us take the hamiltonian

$$\hat{H} = H_0 + V_1(t) + V_2(t) \tag{6.3}$$

Where H_0 is the time-independent hamiltonian with eigenfunctions $\{\varphi_\alpha\}$ and eigenenergies $\{\varepsilon_n\}$ in the Hilbert space α. And $V_1(t)$ and $V_2(t)$ are periodic with period T_1 and T_2 respectively. One approach, detailed in [67, 68, 69] is to apply the same techiniques as we did in chapter 4 to the larger space

$$\alpha \otimes \mathcal{F}_1 \otimes \mathcal{F}_2 \tag{6.4}$$

Where α is the Hilbert space of the original hamiltonian, and $\mathcal{F}_1, \mathcal{F}_2$ are the Fourier spaces

in ω_1 and ω_2 respectively. We shall not go into too much detail about this method, except to say that working in this very large composite Hilbert space makes solving the matrix equation computationally difficult[1].

Instead we will write $k(t)$ as:

$$k(t) = k_0(1 + \gamma_1 \cos(m\Omega t) + \gamma_2 \cos(n\Omega t)). \tag{6.5}$$

Where m,n are co-prime integers. Using this form in our hamiltonian Eq. 6.1, we can view Ω as our drive frequency, and view m, n as multipliers on the drive frequency. This form has the advantage of allowing us to use Eqs. 4.9 and 4.10 to compute the Fourier states. This is because we can now view the hamiltonian as still having a single (albiet longer) period $2\pi/\Omega$. However, this still requires us to increase the number of Fourier terms we have to consider if we want our states to converge. This can be seen if we look at the approximation we obtained for $\mathcal{L}_w$,

$$\mathcal{L}_w = \mathcal{W}/(\hbar\omega) \tag{6.6}$$

It is clear that if $\omega = n\omega'$, then $\mathcal{L}_w = n\mathcal{L'}_w$. This fact limits us to a smaller set of (m, n) values than we would like since our memory requirements scale as $\mathcal{O}(\mathcal{L}_w^2)$. Still, this method is an improvement over the previous approach, since we went from $\mathcal{O}(\mathcal{L}_w^2)$ to $\mathcal{O}(n\mathcal{L}_w)$.

We will still use the operators $\mathcal{D}_\kappa$ and $\mathcal{Y}_\alpha$ to work in the 'co-breathing' frame, so our

[1]For example if we need 100 Fourier terms for a single-frequency to converge, we will need $\approx$ 100times as many terms for the two-frequencies of similar size

hamiltonian after transformation is still

$$H_f = \frac{1}{\kappa^2}\left(\frac{p^2}{2m} + V_\gamma \cos(k_e x)\right) + \frac{mx^2}{2}(\omega^2\kappa^2 + \kappa\ddot{\kappa}) \tag{6.7}$$

except $V_\gamma = (1 + \gamma_1^2/2 + \gamma_2^2/2)V_0$, $k_e = (\sqrt{1 + \gamma_1^2/2 + \gamma_2^2/2})k_0$, and $\kappa = \frac{k_0\sqrt{1+\gamma_1^2/2+\gamma_2^2/2}}{k(t)}$.

Calculating Critical Drive

As seen above, we still have the external harmonic trap term $\omega^2\kappa^2$ in our hamiltonian. This is because even in the two-frequency case, the time-averaged trap without the external harmonic term ends up being anti-trapping. This means that if we want to operate in the critical drive limit, i.e. where the time-averaged trap is zero, we need a way to calculate Ω_c for a given set of γ_1, γ_2, m, n. In other words, we need to find an Ω that satisfies

$$\frac{\Omega}{2\pi}\int_0^{2\pi/\Omega} \omega^2\kappa^2 + \kappa\ddot{\kappa}\ dt = 0. \tag{6.8}$$

For the two-frequency $k(t) = k_0(1 + \gamma_1 \cos\omega_1 t + \gamma_2 \cos\omega_2 t)$, this integral is not solvable analytically. Even the 'simplest' term in this integral (which is just $\omega^2\kappa^2$)

$$a\int_0^{\frac{2\pi}{\Omega}} \frac{1}{(1 + \gamma_1 \cos(m\Omega t) + \gamma_2 \cos(n\Omega t))^2} dt \tag{6.9}$$

has no closed form solution. We are then left looking for numerical methods of computing Ω_c. The integral in Eq. 6.8 is highly oscillatory, so we have to be careful with how we approach this. Since our simulation is written in Python, the first attempt was to use a

simple bisection algorithm using integration methods provided by SciPy. This simply uses the fact that given a continuous function $f(x)$ over an interval $[a, b]$ where $f(a) < 0 < f(b)$, there exists $c \in [a, b]$ for which $f(c) = 0$[2]. The algorithm in pseudocode is

Data: f(x),a,b, ϵ

Result: c such that $f(c) < |\epsilon|$

c = $\frac{(a+b)}{2}$;

while $|f(c)| > |\epsilon|$ do

    if sgn($f(c)$) = sgn($f(a)$) then
        a=c

    else
        b=c

    end

    c = $\frac{a+b}{2}$

end

Output: c

Where sgn is the sign function. This algorithm works by taking the interval $[a, b]$, looking at the function at its midpoint c, and depending on the sign and value of $f(c)$ either changing the interval(to $[a, c]$ or $[c, b]$) or, if the error is small enough, returning c as the required output. This algorithm has the advantage of being quick[3]. The problem we face with this method is that the SciPy integration routines do not converge sufficiently quickly, and even when they do, the Ω_c we obtain end up being inaccurate. This problem persisted even if we used other packages for numerical integration (for example MPMATH).

[2]This is the Intermediate-Value Theorem

[3]The upper bound for runtime is $N \leq \log_2 \frac{|a-b|}{\epsilon}$

Only the integrals calculated using Mathematica[70], gave values of Ω_c that were correct when checked. Thankfully, there is a package called 'Wolfram Client Library' which lets us use Mathematica from within Python.The Python code parses the simulation settings, and then calls Mathematica sub-routines to compute the value of Ω_c.

We would like to note the curious fact that it is usually faster to compute the integral

$$\frac{\Omega}{2\pi}\int_0^{2\pi/\Omega} \omega^2\kappa + \kappa\ddot{\kappa} + 1 \; dt \tag{6.10}$$

And find Ω_c such that this integral evaluates to 1. The final thing to note is that there are sometimes multiple values of Ω_c that satisfy Eq. 6.8, and we always try to take the lowest of those values. We do this by checking if we can find a $x < \Omega_c$ where the sign of $f(x)$ changes. Since we do not have the closed form of the integral, we cannot prove that the Ω_c we found is the lowest. But we are fairly confident of that being the case.

Fourier Coefficients

To be able to use Eq. 4.10, we need to compute the Fourier coefficients of our Hamiltonian. Since we need both negative and positive coefficients, we will be using the exponential form of the Fourier series

$$H_f = \sum_{m=-\infty}^{\infty} H_f^{(m)} e^{im\Omega t} \tag{6.11}$$

Where

$$H_f^{(m)} = \frac{\Omega}{2\pi}\int_0^{\frac{2\pi}{\Omega}} H_f e^{-im\Omega t} dt \tag{6.12}$$

Since we already knew that numerically integrating oscillatory functions might be difficult in python, we again used Mathematica to compute the coefficients. Then we can construct our matrix equation and solve for the Floquet states.

Simulation Limits

Before we move on to the results, let us discuss the parameters of our simulation. As we saw earlier, using $m\Omega$ and $n\Omega$ to mimic as single frequency hamiltonian requires us to include n times as many terms to ensure that our system converges[4]. This has a cascading effect on the memory requirements and runtime and limits us to n, m being small integers. As such we mostly ran simulations for $(n, m) < 10$, with the largest being $n = 7, m = 5$. Even here, in the case of $(7, 5)$ we were using ≈ 100 GB of memory. So it seems unlikely that this method could be used for $n/m \gg 1$, as even for $n = 22, m = 7$, we are looking at $30 - 50$ times the memory and runtime requirements for $n = 3, m = 2$. Our amplitudes γ_1, γ_2 were $.001 < \gamma_1, \gamma_2 < .2$. And for all simulations our lattice had $j = 33$ sites, and the external trap frequency $\omega = 20\text{Hz}$[5].

Convergence and grouping states

Filtering states in the two-dimensional case proceeds as it did in the single-frequency case. We use Eq. 5.59 to find ϵ_{rms} and then perform direct numeric integration to further refine our results. The only difference is , as we mentioned, the larger memory and runtime

[4]Without loss of generality, we can assume $n > m$

[5]This is because we don't expect the absolute value of ω to effect the results, similarly for the absolute value of j. Increasing j also runs into the same problem as large (m, n) since the simulation scales in size with j^2.

requirements.

As mentioned earlier, finding the first Fourier-Brillouin zone is not as straightforward. We still compute Q_d, and follow the same procedure for demarcating the different states. But we do not always get j distinct states. Sometimes the number is much larger, and other times it is smaller. Let us discuss each of these scenarios

In the first case, our procedure is giving us more distinct states than we expect. To understand this let's take an example, where $\gamma_1 = .05, \gamma_2 = .01, m = 2, n = 3$ as our simulation parameters. Following our procedure gives us ≈ 200 distinct states, which is far more than the expected 33. What this implies that after we have constructed and sorted Q_d, we have found ≈ 200 locations where $|\delta_n| > |\epsilon|$ ($\delta_n = q_{n+1} - q_n$). Now, the distance between these locations is the number of states with the same quasi energy mod $\hbar\omega$. In other words, this is the number of different Fourier m-blocks a distinct physical state re-occurs in, let's call this m_j for each distinct j. If a state only appeared in very few m-blocks, ($m_j < 3$), then it is likely to not be physical. If add this additional condition of $m_j \geq 3$, we find that in this specific case, we are left with the correct number (33) of states, each with $m_j > 20$, confirming the validity of this method[6].

In the second case, we are getting fewer states than we expect. This is easy to understand, it just means that we have degenerate states in our first Fourier-Brillouin zone. Since we group our states using energies, this is not a surprising outcome. We can correct this by looking at each group, and computing the overlaps at $t = 0$.

$$\langle \psi_{g,i}(t) | \psi_{g,i'}(t) \rangle \tag{6.13}$$

[6]There are rare cases where after doing this filtering, we are left with fewer than the number of states we expect. Those are discussed below

where $\psi_{g,i}$ denotes the i^{th} state in group g. Between different, but degenerate states, we expect the overlap to be zero. For non-zero overlaps ($> .5$), we can be fairly sure that those states represent the same physical state. We then repeat this procedure for all the groups, and find our 'missing' states.

Between these two methods, we can ensure that we identify all the physically distinct states[7].

6.4 Results

We will group our results into distinct sections by particular facet of behaviour were think are exhibiting.

6.4.1 Γ-dependent tunnelling modification

This is the first scan we performed, scanning over $\Gamma = \frac{\gamma 2}{\gamma_1}$ for a given set of drive multipliers (m, n). This scan was to explore the relationship between the ratio of amplitudes of the two breathing lattices and nearest neighbour tunnelling. We wanted to see if our intuition about Γ was correct, namely that for $\Gamma \ll 1$ and $\Gamma > 1$ our results are similar to those for a singel frequency, and that we would see maximal deviation from the single frequency behaviour at $\Gamma \approx 1$ The pair $m = 2, n = 3$ closely match our intuition, as shown in fig. 6.1, we can see how the tunnelling rate J_0 starts out identical to the single-frequency scenario for $\Gamma << 1$, and shows maximal deviations from this behaviour at $\Gamma \approx 1$. For $\Gamma > 1$, as expected, the behaviour look similar to $\Gamma \ll 1$. This repeats for other m, n pairs

[7] There were a few occasions where both methods were required, and in those cases they were conducted in the order presented here

[$(m, n) = (3, 4)$ and $(m, n) = (3, 5)$, as seen in fig. 6.2 and fig. 6.3 (We have not shown the $\Gamma \ll 1$ plots, as they all look like fig. 6.1a).

(a) $\Gamma \ll 1$

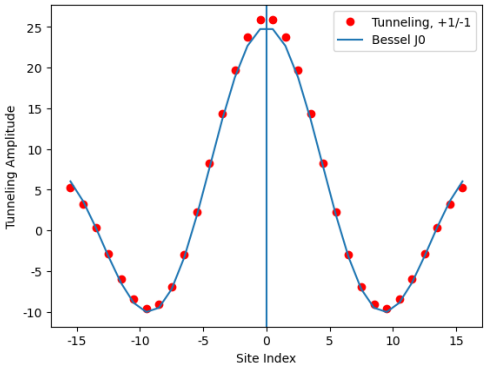

(b) $\Gamma \approx 1$

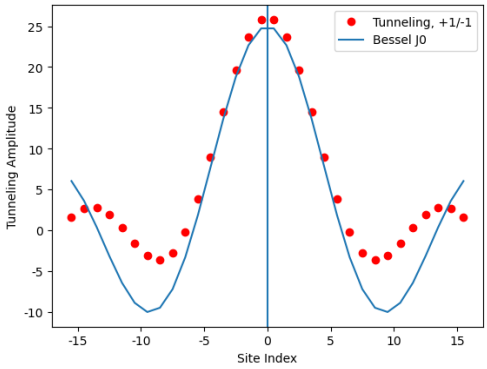

(c) $\Gamma > 1$

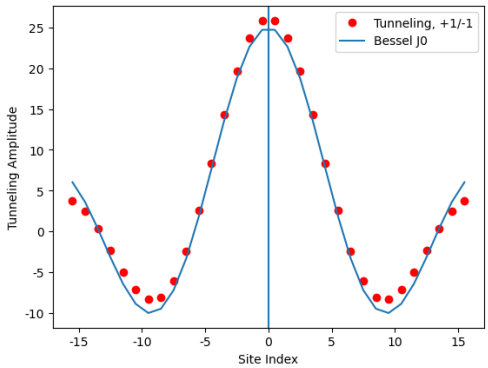

Figure 6.1: Nearest neighbour tunnelling amplitude as a function of site index for three different Γ value for $m = 2, n = 3$. (a) shows the tunnelling for $\gamma_1 = .05$ $\gamma_2 = .005$. (b) shows the tunnelling for $\gamma_1 = .05$ $\gamma_2 = .045$, and (c) is for $\gamma_1 = .02$, $\gamma_2 = .07$

6.4.2 Modifications from R

While we were unable to conclude on whether Aubry-André like behaviour arises from modifying R, we did not a difference between integer and non-integer values of R. Below are the of plots comparing Γ scans for $3, 2$, $2, 1$ and $3, 1$. While we see the same behaviour modifications, it is far more pronounced in the non-integer R. Both the deviation from the

(a) $\Gamma = .5$ (b) $\Gamma = 3.5$

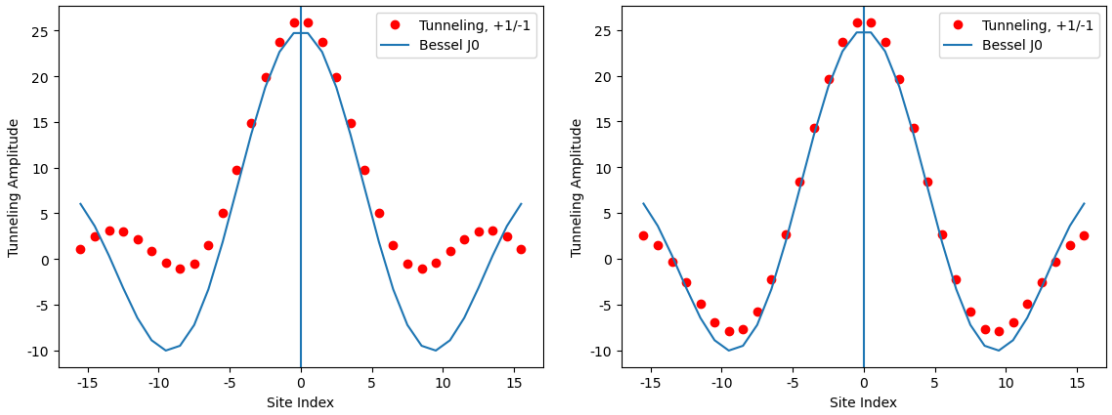

Figure 6.2: Tunnelling plot for $m = 3, n = 4$

(a) $\Gamma = .5$ (b) $\Gamma = 2.5$

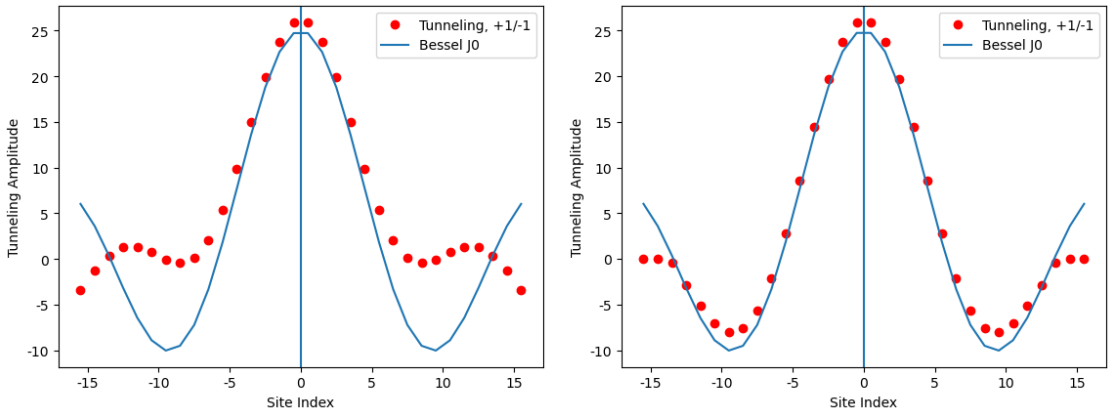

Figure 6.3: Tunnelling plot for $m = 3, n = 5$

$\mathcal{J}_0$, and the range of Γ values where this deviation is present are much smaller.

We are not sure of the origin of this distinction, but we suspect it arises from the fact for non-integer R, there are terms in our Fourier series that are not harmonics of either of our frequencies. For example, in the matrix equation for $3, 2$, the Fourier terms (and the associated Floquet m-blocks) for $i = 5, 7, 11$ etc. are not harmonics for either 3Ω or 2Ω. If the R is an integer, this is not the case, as Ω is one of the driving frequencies.

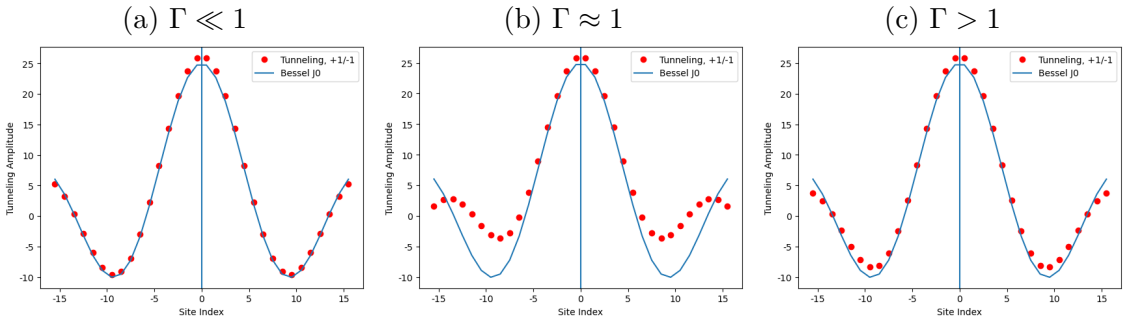

Figure 6.4: Γ scan for $m = 2, n = 3$

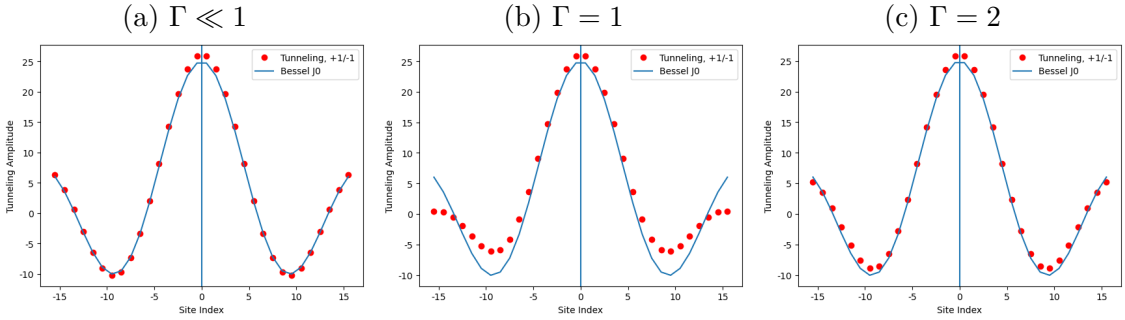

Figure 6.5: Γ scan for $m = 1, n = 2$

6.4.3 Emergence of divergent behaviour

All our results so far can be viewed as perturbations of the single-frequency breathing behaviour. The second frequency's effect become more apparent as we move away from the center, and the modulation increases. This can be seen clearly in fig. 6.7. However, for certain combinations of the parameters, this was no longer the case. Instead we saw a large shift in the tunnelling amplitude at the lattice centre. An example is given in fig. 6.8

In contrast to the earlier results, the effective hamiltonians (fig. 6.9) here show higher-order coupling near the centre. This is not something we were expecting, and a survey of recent literature has shown no similar results. This is even more surprising when we consider

(a) $\Gamma \ll 1$ (b) $\Gamma = 1$ (c) $\Gamma = 2$

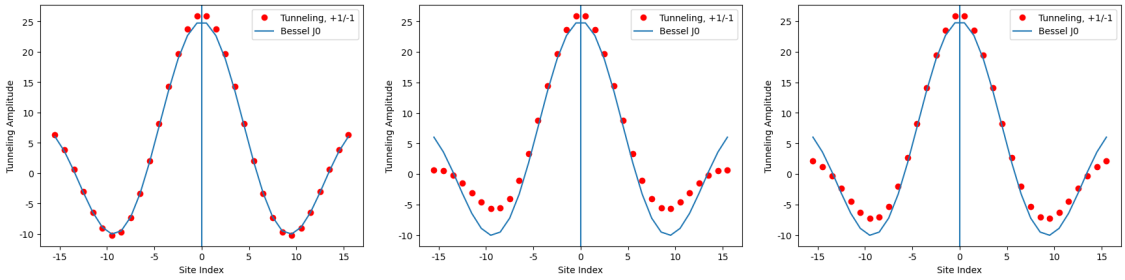

Figure 6.6: Γ scan for $m = 1, n = 3$

the fact that the center experiences the least amount of motion from the breathing lattice. We expect deviations to arise where the effect of the breathing lattice is felt most strongly by the atoms, but here we have the opposite happening. As such, we sought to characterise this behaviour and look for patterns.

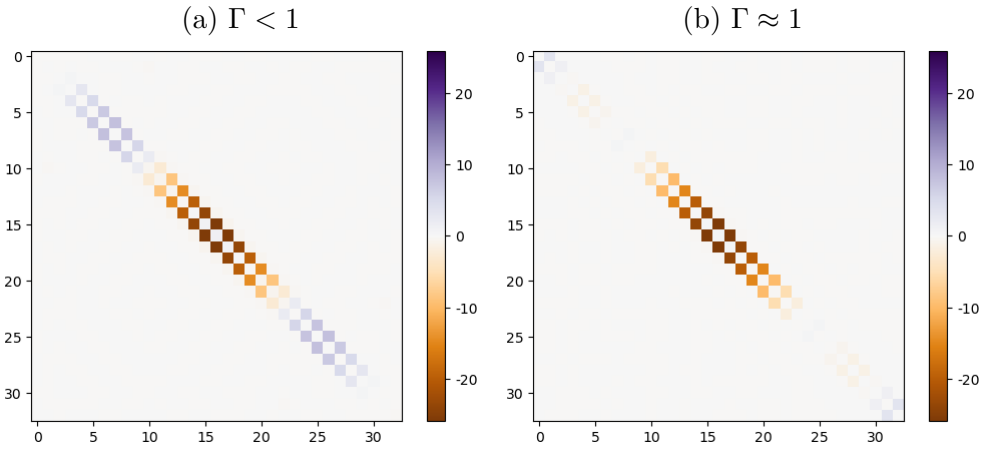

Figure 6.7: Plot contrasting the effective Hamiltonian of $\Gamma < 1$ with $\Gamma \approx 1$, showing the couplings between the different lattice sites. For both $\Gamma < 1$ and $\Gamma \approx 1$, we only have nearest neighbour coupling. And they show the $\mathcal{J}_0$ tunnelling exhibited by $\Gamma < 1$, and the deviation from it for $\Gamma \approx 1$. It is important to note that the deviation occurs towards the edges of the lattice, leaving the center relatively unperturbed

Table 6.1: Range over which behaviour like fig. 6.8 was observed.

(γ_1, γ_2)	(m, n)	Ω_c
(.007, .002)	(3,5)	78.38 Hz
(.03, .02)	(3,4)	210.55 Hz
(.1, .2)	(2,3)	565.40 Hz

We saw this behavior repeat over a large range of parameters. There was no discernible relationship to Γ, R or even Ω_c. This can be be seen by looking at table 6.1, which shows the large range of parameters over which this behaviour can be seen. Looking at a scan near these values, we observed that this phenomena, in contrast to the normal two-frequency results, first begins to occur at the lattice centre (fig. 6.10a).

We have arranged the various stages of this in fig. 6.11, and have labelled them with ϑ, which is just a normalized deviation of our tunnelling from $\mathcal{J}_0(0)$

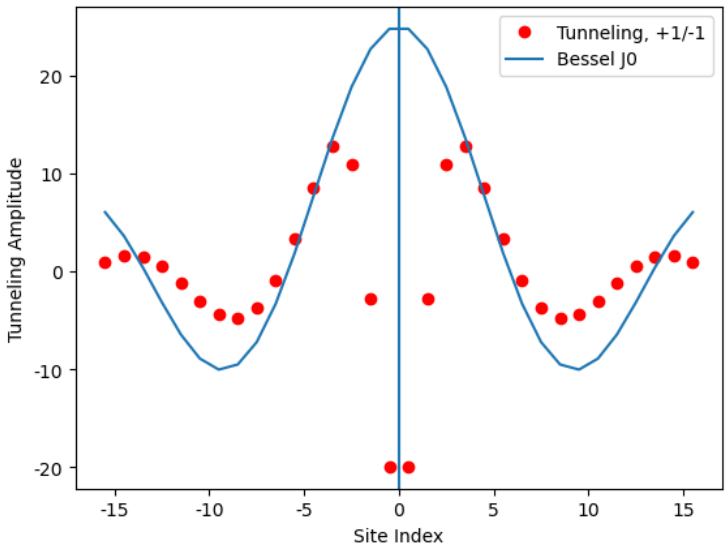

Figure 6.8: Tunnelling plot for $m = 2, n = 3$ at $\gamma_1 = .12$ and $\gamma_2 = .2$

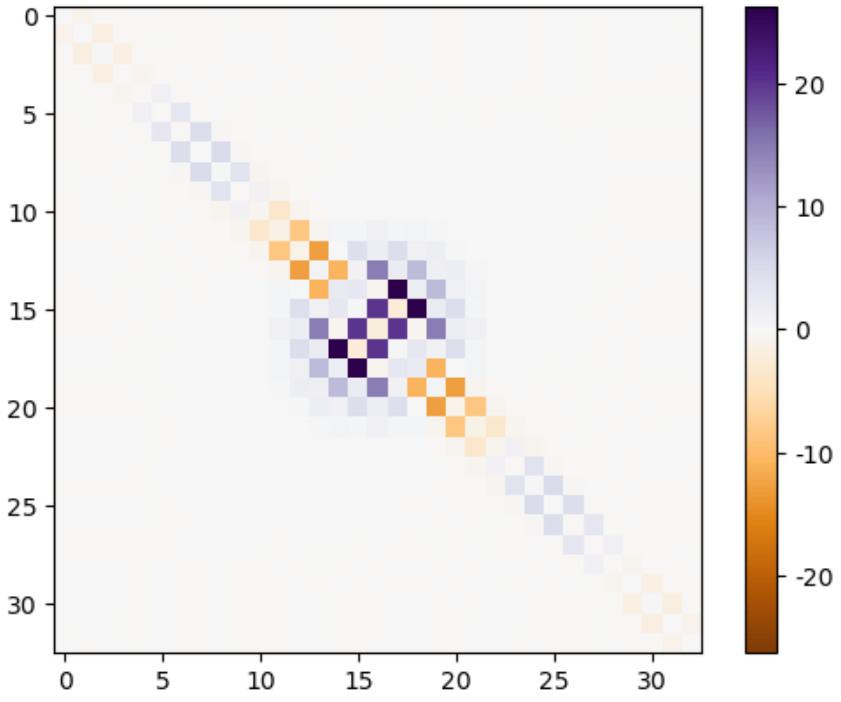

Figure 6.9: Effective Hamiltonian for fig. 6.8

(a) Tunnelling plot showing the first appearance of the central dip

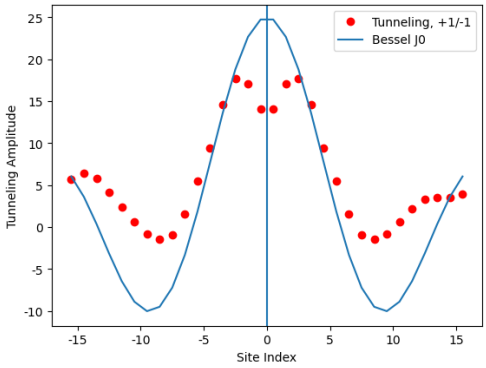

(b) Effective Hamiltonian

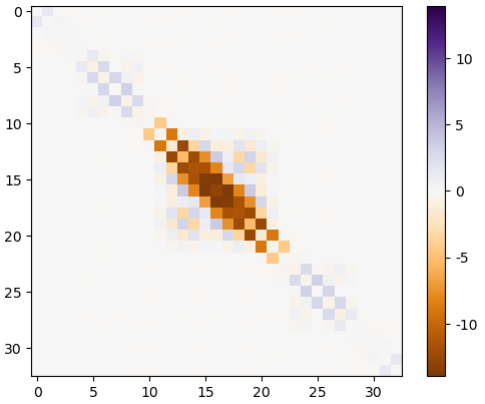

Figure 6.10: Plot showing the onset of higher-order couplings

(a) $\vartheta = 0$

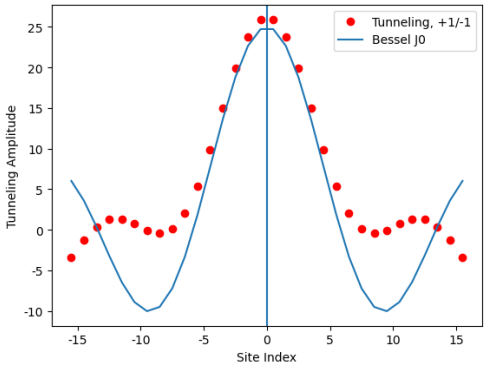

(b) $\vartheta = -.3$

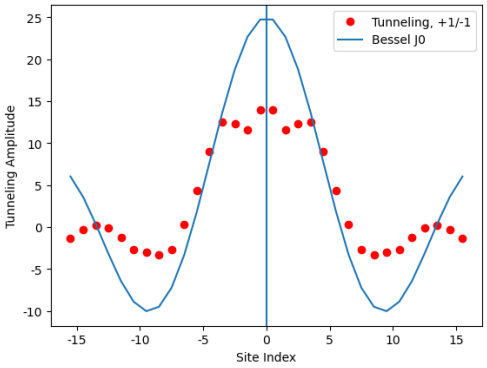

(c) $\vartheta = -.35$

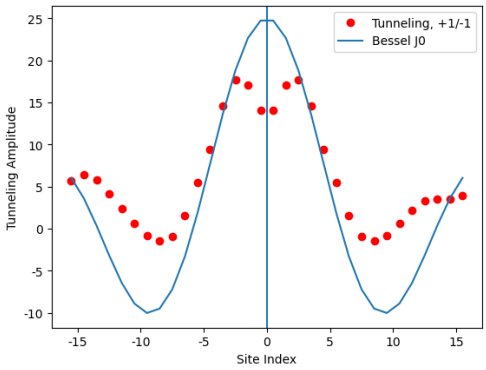

(d) $\vartheta = -.6$

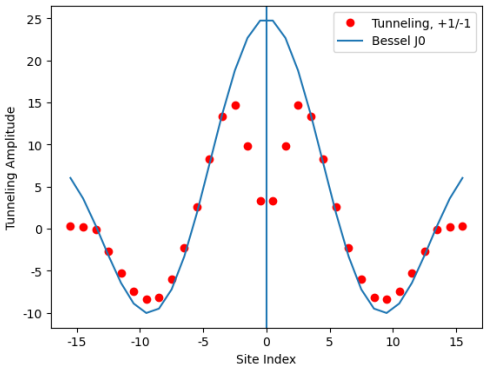

(e) $\vartheta = -1$

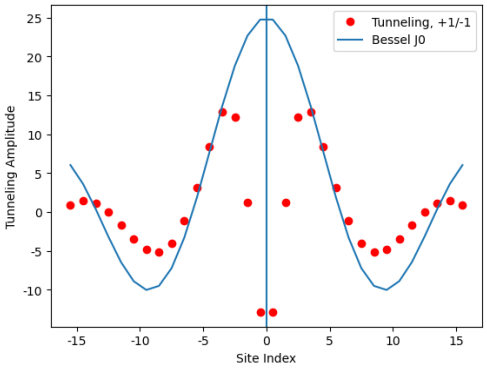

Figure 6.11: Progression of divergent tunnelling, characterised by $\vartheta = \frac{J(0)-\mathcal{J}_0(0)}{|\min(J(0))-\mathcal{J}_0(0)|}$

6.4.4 Analysis and possible sources of this phenomena

As we stated earlier, we have not been able to find a relationship between ϑ and the other parameters of the simulation $(\gamma_1, \gamma_2, m, n)$. It doesn't have a simple relationship to Ω_c, so we cannot say that it a low/high frequency effect or resonance. It does not depend on the ratio R, as we are able to modulate ϑ by modulating Γ while keeping R constant. We suspect a similar relationship exists in other direction, but we are limited by the small set (m, n) that are computaionally feasible.

6.4.4.1 Phase and Symmetry

One unexplored possibility is that this is a consequence of the relative (starting) phase between the two frequencies. In our formulation of $k(t) = k_0(1+\gamma_1 \cos(m\Omega t)+\gamma_2 \cos(n\Omega t))$, we assumed to the phase between frequencies to be zero. We could a phase (ϕ) to this, i.e.

$$k'(t) = k_0(1 + \gamma_1 \cos(m\Omega t) + \gamma_2 \cos(n\Omega t + \phi)). \tag{6.14}$$

This hypothesis is helped by the fact that if we look at expansions of $k(t)$ and $k'(t)$ around Ω and ϕ respectively, we get the same first order term

$$k^{(0)}(t) = (\gamma_1 + \gamma_2 + 1)\, k_0 + \Omega^2 \left(-\frac{1}{2} \left(k_0 \left(\gamma_1 m^2 + n^2 \gamma_2 \right) \right) t^2 \right) + \Omega^4 \left(\frac{1}{24} k_0 \left(\gamma_1 m^4 + n^4 \gamma_2 \right) t^4 \right) \tag{6.15}$$

This suggests that a change in the critical frequency Ω_c is akin to shift in the phaseϕ. Recent work in multi-mode Floquet dynamics ([71] [72] [73]) has emphasised the importance of

this relative phase, so we suspect this is a good place to start.

Having thought more about the role of phase, we now consider it to be an unlikely explanation. The best way to understand this is to consider what happens to $k(t)$ when we add a phase. When $\phi = 0$, $k(t)$ is an even function. By extension, this implies that our hamiltonian H_{br} is an even function. Setting $\phi \neq 0$ turns $k(t)$ into a function that is neither even nor odd. The more practical consequence of this is that now we need twice as much memory for our Floquet hamiltonian. This is because an even function can be written as a Fourier series with only real coefficients, but for functions that are neither even nor odd, the coefficients are complex. And quite trivially, all else being equal, going from real-valued to complex-valued matrices doubles memory requirements. The other objection this raises is more fundamental. It seems unlikely that behaviour exhibited by a Hamiltonian would be caused by it behaving as if it had lost a symmetry still present in the system.

6.5 Experimental plan and potential challenges

Now that we've gone over our theoretical results, and what kind of behaviour we could expect in the single-frequency and two-frequency case, it is a good place to discuss the planned breathing lattice experiment. The HiBAL worked by combining beams from two wide bandwidth AOMs to generate a shallow angle lattice. The frequency of the RF going into the AOM controls how far the first order beam is deflected, which in turn changes the angle at which the beams intersect, which by eq. (2.8) changes the lattice period. By carefully controlling how we modulate this RF signal, we could create a time-varying potential. To replicate the form of $k(t)$ we have been using, we would just need a

linear modulation of the RF signal used to drive the AOMs. The two AOMs in our setup were controlled by two different AWGs, where one is a 'leader' and the other is a 'follower' to ensure no relative phase shift in between the two signals. By choosing an appropriate waveform to store in the AWG, we can generate a breathing lattice.

There are many ways to achieve this, but what I had planned was to use a microcontroller connected to the experimental control computer. This would be attached to a direct-digital synthesiser(DDS), like the AD9910, which would generate the waveform that would be fed to the AWGs. In the case of the single-frequency breathing lattice, we would just simply give the microcontroller the desired γ or Ω_c, after which the microcontroller would use to compute the other and generate the requisite waveform. There are, however, many unknowns here. To generate the disordered lattice we used to investigate Griffiths' physics, we rapidly pulsed a set of discrete frequencies. The pulse lengths were chosen such that the atoms effectively saw all the frequencies at the same time, hence generating the disordered potential. For a breathing lattice we would need a continuously varying signal. One potential problem that could arise would be that the AWGs simply don't have enough resolution, or we might be severely limited in the range of frequencies we could investigate. One problem we did solve while building the HiBAL was phase-locking, we used a Mach-Zender interferometer along with a piezo-mounted mirror to ensure the two beams stayed phase locked. The other point of concern is the AOMs themselves, as we had not yet tested their response to a continuos frequency modulation. It is possible that one of them a slightly longer delay while changing frequencies, and so that would be something we would have to consider.

The biggest challenge potentially would be the measurement itself, as we are not sure

how an actual BEC would differ from our clean model. In the lab we do not have the luxury of turning off interactions, or of ensuring that every experimental shot is identical. Either of these could mask the effect of the breathing lattice, especially in one-frequency, which was the original plan.

6.6 Future Work

We demonstrated the presence of an unexpected modification to the tunnelling behaviour of the breathing lattice. There many directions that this work could be extended, in both the numerical and theoretical sides.

On the theoretical side, it would be interesting to see if treating ϑ as a dynamical variable could give us insights into the behaviour.

On the numerical side, we are mostly limited by the computing power available in what can be done. It would be very interesting if it would be possible to investigate frequencies with much larger Γ values. As mentioned, one of our initial goals was to see if there was any Aubry-André like phenomena in the two frequency system. We wanted to see if there was a qualitative change in behaviour as we changed (m, n) from less to more incommensurate, for example a sequence approaching $\frac{1}{\sqrt{2}}$: $[(2,3), \ldots (5,7), \ldots (70,99), \ldots]$. Unfortunately, due to the polynomial increase in memory required to adequately test this hypothesis, all we are able to say is that there is a difference between Γ as an integer and as a rational number. But the question of whether there is a marked difference between $(m, n) = (5, 7)$ and $(m, n) = (70, 99)$ remains very much open.

Furthermore, there still remains a large parameter space that is unexplored. Perhaps there is even more exotic behaviour that exists for certain value of (m, n) and Ω_c.

The challenge in pursuing either of these avenues is computational power. For $(m, n) = (70, 99)$ the Floquet matrix already consumes ≈ 40 Terabytes of RAM. This is in addition to needing at least an order of magnitude more storage than that. There is some leeway to investigate more efficient ways of storing these matrices, by using sparse

data structures for example, but you still run into the problem of polynomial scaling.

And of course, if someone were to conduct this experiment, comparing their results with our predictions could prove very interesting.

Chapter 7: Conclusion

We introduced BECs, and briefly discussed their generation in a lab setting. We then discussed the features of our lab, including our power lattice generation apparatus, that made the investigation of a breathing lattice system possible.

We then presented an overview of the work done for a single frequency breathing lattice, and the presence of Bessel $\mathcal{J}_0$ tunnelling. We briefly discussed how we verified the single-band nature of our simulations, and then turned our focus to the two-frequency case.

We then discussed our extension of the breathing lattice to two frequencies, and the results we obtained. For most of the two frequency values we presented, their results could be viewed as perturbations on the single frequency case. However, we showed that there are some 'islands' of radically different behaviour. Of special interest was modifications to tunnelling at the lattice centre, and the emergence of beyond nearest-neighbour couplings.

We found that this anomalous behaviour does not correlate well with any simulation parameter. It does not appear to depend on a energy scale, and it appears at seemingly random R and Γ values. Symmetry considerations make phase unlikely as an explanation, so we are left looking for more complex explanations.

Appendix A: Publication: Griffiths Physics in an Ultracold Bose Gas

Note: The following is the text of work published by our group in PRA adjusted in format only to comply with style requirements.

A.1 Abstract

Coupled XY model systems consisting of three-dimensional (3D) systems with disordered interlayer physics are of significant theoretical interest. We realize a set of coupled quasi-2D layers of ^{87}Rb in the presence of disordered interlayer coupling. This is achieved with our high bandwidth arbitrary optical lattice to obviate restrictions on the dimensionality of disorder with speckle-generated optical fields. We identify phase crossover regions compatible with the existence of a pair of intermediate Griffiths phases between a thermal state and the emergence of bulk 3D superfluidity.

A.2 Introduction

The intersection of dimensionality and disorder is a rich area of study in condensed-matter physics. The precise control of disorder available with optical potentials enables the realization of well characterized disordered systems with quantum degenerate atomic gases. Optical speckle has been used to generate disorder for one-, two-, and three-dimensional

systems [74, 75, 76], exhibiting Anderson localization, a disordered Berezinskii-Kosterlitz-Thouless (BKT) transition [77], mobility edges in three dimensions [78], and emergence of a Bose glass [79]. Similarly, quasidisorder provided by incommensurate lattices has been used to realize the Aubry-André model in the presence of interactions [80], the role of quasi-disorder in adiabaticity [81], to study many-body localization [82], and has been contrasted against uncorrelated disorder in transport [83].

While two-dimensional (2D) Bose gases in isolation are well described by BKT physics [84] (approximated by the XY model), recent theoretical work [32, 85, 86] suggests rich behavior when layers of such systems (including stacks of 2D superfluids, cuprate superconductors, and planar magnets) are randomly coupled to one another. They are predicted to exhibit Griffiths physics [87, 88, 89] when the interlayer couplings or layer thicknesses are subject to uncorrelated disorder. A pair of phases of matter emerge as the temperature is lowered from a nondegenerate state to bulk 3D order (Bose-Einstein condensate, magnetization, or superconduction). Each intermediate phase is a Griffiths phase, with properties dominated by the most extreme local deviation in the disordered system. The first is an anomalous Griffiths phase, a class of sliding phase [90] that exhibits 2D order (superfluidity, magnetic susceptibility, or superconduction). The second is a semiordered Griffiths phase where order appears in the third dimension. (Magnetic Griffiths phases have recently been observed in bulk metal alloy systems [91, 92], but not in anisotropic systems.)

References [32, 85, 86] employ the phase stiffness ρ_s^x along a direction e_x to characterize the Griffiths phases. Phase stiffness is a measure of the energy required to impose a phase difference ϕ_x between two ends of a finite system. As a function of system size L and

system energy E, the phase stiffness is defined as

$$\rho_s^x = \frac{1}{L}\frac{d^2E(\phi_x)}{d\phi_x^2}. \tag{A.1}$$

While a computationally convenient parameter, it is not easily measurable in experimental atomic systems. Although it is possible to measure the critical velocities of superfluids [93], these disordered systems are predicted to have very small superfluid fractions and critical velocities over much of the phase diagram. Instead we use an analysis of the fluctuations in large data sets of time-of-flight (TOF) momentum distributions to gain information about the phases as a function of temperature and lattice depth.

We associate the appearance of a Thomas-Fermi-like distribution in the two in-plane dimensions ($p_\parallel$) paired with a thermal distribution in the third ($p_\perp$) with a 2D superfluid transition at ∼200 nK. As we decrease the temperature we observe the emergence of discrete modes in fluctuation correlations along $p_\perp$ [94], which may characterize the expanding length-scales of superfluid puddles in the anomalous Griffiths phase. Finally we interpret the suppression of zero momentum atomic density fluctuations at our lowest temperatures with the Bose statistics of macroscopically occupied non-local state, an observation consistent with 3D superfluidity.

A.3 Experimental Approach

We study this system using optical potentials generated for a cloud of ultracold ^{87}Rb. After initial loading and cooling, the atoms are held in vacuum by a pair of optical tweezers. There they are subjected to a disordered 1D optical potential from an optical

lattice generation system. They are further cooled via optical evaporation to temperatures from 10 nK to (numerical range) 250 nK. This temperature range spans both thermal and degenerate states of the atomic cloud. After some evolution time in the lattice, we release the atoms from all optical fields to expand ballistically. They form a position distribution determined by their momentum distribution at the time of release. This is repeated many times, allowing us to study statistics of the measured momentum distributions. Each part of this process is discussed in more detail below.

We create degenerate gases of ^{87}Rb using a hybrid magnetic trap-optical dipole trap [95], which then loads into a dipole trap whose waist is translated 30 cm into a science chamber. The atoms are finally loaded into a crossed 1550 nm dipole trap and disordered optical lattice, and evaporatively cooled in the $F = 1$, $m_F = -1$ state. Final trapping frequencies ($\nu_\parallel$, $\nu_\perp$) are $E/2\pi\hbar$ = (100.0, 20.0) Hz at our lowest temperatures and (126.5, 25.3) Hz at our highest.

Evaporation begins with a nondegenerate cloud in the presence of our high bandwidth arbitrary lattice (HiBAL) (see A.1). (Disorder generated using optical speckle necessarily includes variations along the propagation direction [1], so the HiBAL was developed to provide the desired potentials.) We Fourier synthesize a potential $U = \sum_j A_j \sin(k_j x + \phi_j)$ from multiple optical lattices spanning two octaves of spatial frequencies. We produce a time-averaged disordered 1D optical potential using 802 nm light with a set of seven shallow angle lattices of incommensurate period ranging from 1.21 µm to (numerical range) 4.70 µm. The 1.21 µm (base) lattice is phase stabilized to an rms of 6(1) mrad with a Mach-Zehnder

[1] For 1D speckle disorder to be feasible, the Rayleigh range must be much larger than the cloud size. Our clouds are on the order of ≈10 µm–100 µm, whereas for a speckle with features and wavelength ≈1 µm, the Rayleigh range ($z_R = \pi w^2/\lambda$) is 4 µm.

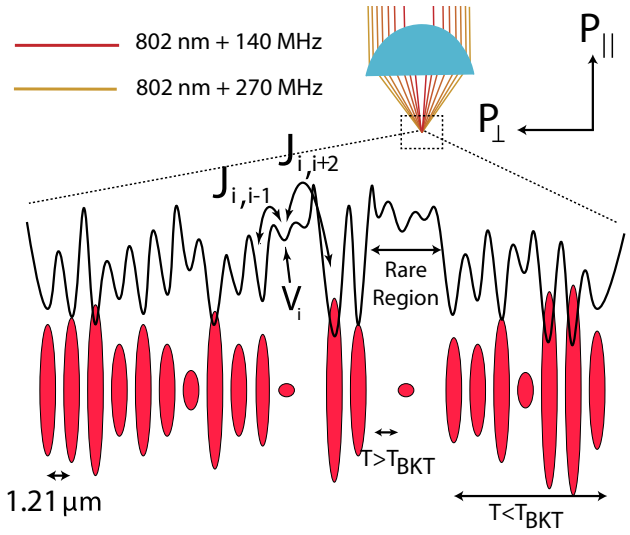

Figure A.1: We engineer a stack of superfluid pancakes with a set of phase-stabilized shallow-angle lattices formed by our HiBAL. Its set of phase-stabilized parallel beams is focused through an aspheric lens to create the 1D disordered optical potential. The local minima have different depths, which generates a local phase space density for each pancake. Interplane hopping $J_{i,j}$ is subject to disorder as well, matching our system most closely with Ref. [85].

interferometer and a piezoelectric transducer-mounted mirror. We confirm the costability of the other optical lattices to our base lattice and our atoms through our diffraction limited 0.5-NA, 22.8× microscope to 19(3) mrad rms. Each lattice pulse is 300 ns in duration. The longest delay between base lattice pulses is 600 ns, and the pulse sequence repetition rate is 3 µs. We use two disordered lattice depths, labeled by the base lattice depth (2.8 kHz and 5.6 kHz). The summed average depth of all seven lattices is 3 times deeper, with an rms deviation equal to the base lattice depth. Our deeper base lattice depth corresponds to 14 effective recoil energies ($E_R/2\pi\hbar = 0.4$ kHz). The rapid pulse rates of our lattices compared to their energy gaps puts us well within the time-averaged potential limit. We observe no differences in heating or TOF images between constant and stroboscopic lattices, thus do not need to consider Floquet physics effects. Shot-to-shot variation in the position of our harmonic 1550 nm trap is sub-µm, and the fastest systematic drift during evaporation is

$6\,\mu\mathrm{m\,s}^{-1}$, which corresponds to energies too small to drive excitations.

The quasi-2D regime in cold gases is reached when the fractional occupation of out-of-plane excited states in an effective, local harmonic oscillator is small. This occurs when the thermal energy scale k_BT is smaller than the harmonic oscillator level spacing $\hbar\omega$, or alternatively when the thermal deBroglie wavelength λ_{dB} is larger than the spatial extent $\sqrt{2\pi}a_z$ where a_z is the harmonic oscillator length [84]. As described above, our disordered lattice has sites with varying depths. For our mean site depth of the shallow lattice ($3\times 2.8\,\mathrm{kHz} = 8.4\,\mathrm{kHz}$) together with the base lattice spacing, we have $k_BT/(\hbar\omega_\perp) \leq 1$ for $T \leq 250\,\mathrm{nK}$, putting us in the quasi-2D regime throughout.

In this regime, our time-averaged Hamiltonian under the local density approximation is

$$\hat{H} = \sum_i \left[\frac{\hat{p}_\parallel^2}{2m} + V_i - \left(\sum_j \frac{1}{2} J_{i,j} \psi_i^\dagger \psi_j \right) + \tilde{g}_i \psi_i \psi_i^\dagger + \frac{1}{2} m\omega_i^2 \left(x^2 + y^2\right) \right], \tag{A.2}$$

where $\hat{p}_\parallel^2/2m$ is the in-plane kinetic energy, V_i is the lattice well depth, $J_{i,j}$ is the hopping strength between two lattice sites i and j, $\tilde{g}_i$ is the scaled quasi-2D self-energy term for each pancake, ω_i is the in-plane trapping frequency, which includes small variations due to the disorder [2].

We prepare gases ranging in temperature from 250 nK down to 25 nK in our lattice potentials. The relative phases of our component lattices are arbitrarily tunable. We chose two sets of relative phases to create two different optical potentials with similar statistics. We observe no difference in the results between the two potentials, confirming that our atom

[2] The out-of-plane momentum $p_\perp$ is contained in the $J_{i,j}$ and $\tilde{g}_i$ terms of the Hamiltonian.

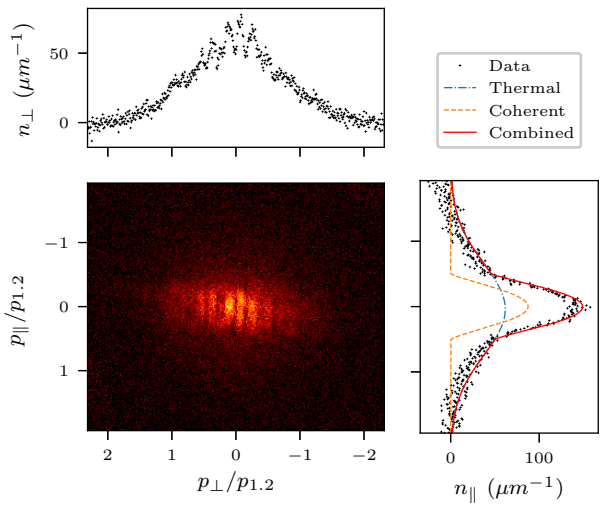

Figure A.2: An example image from a 112 nK cloud in our 2.8 kHz lattice, shown together with the distributions $n_\perp$ and $n_\parallel$ for that image. Momenta are given in units of the recoil momentum of our shortest period lattice, $p_{1.2}$. The bimodal fit to $n_\parallel$ is displayed as a solid red line, with the thermal and coherent parts of the fit displayed separately as a blue dot dashed and orange dotted lines, respectively.

cloud is large enough (greater than 70 pancakes) to average over the disorder. Each data set contains two different hold times, 200 ms and 4 s, which show no statistical difference, indicating equilibrium.

We levitate our atoms during 47 ms of TOF with the use of a gravity-canceling magnetic coil with a microsecond switching time to resolve the momentum distributions $n(p_\parallel, p_\perp)$. Gross-Pitaevskii simulations show that our distributions along the disordered direction, $p_\perp$, are minimally distorted by interactions during the expansion due to the rapid expansion of each atomic plane. We conclude that our TOF distributions faithfully represent the momentum distribution along the disordered direction.

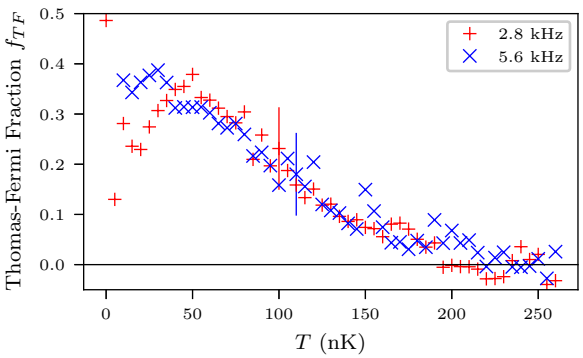

Figure A.3: The fraction of atoms in the Thomas-Fermi distribution, f_{TF}, is plotted as a function of temperature. The shallow lattice is plotted with red +'s, and the deep lattice with blue ×'s. Error bars are the standard deviations of the fractions in each bin, and a typical bar is shown near the center for each lattice depth. We remove a baseline value of 0.054, a fit artifact, from the Thomas-Fermi fraction. f_{TF} is consistent with zero at high temperatures, but increases to finite values as early as 200 nK, establishing $\rho_s^{\parallel} > 0$ below 200 nK.

A.4 Analysis

The trapping energies along the disorder and in plane differ by over a factor of 85, causing each direction to expand at very different rates. The expansion from the tightest direction of confinement will quickly reduce the local density, preventing any interactions that might have otherwise coupled $p_{\parallel}$ and $p_{\perp}$ during the ballistic expansion phase. Therefore we treat their momentum distributions as separable. We focus on the in-plane and longitudinal momentum distributions, $n_{\parallel}(p) = \sum_{p_{\perp}} n(p_{\parallel}, p_{\perp})$ and $n_{\perp}(p) = \sum_{p_{\parallel}} n(p_{\parallel}, p_{\perp})$. At high temperatures $n(p_{\parallel})$ is a Gaussian. As the temperature drops a bimodal distribution emerges, a thermal distribution plus a Thomas-Fermi-like distribution as expected after expansion [96]. An example image is shown in A.2. We apply a bimodal fit to $n(p_{\parallel})$ for every cloud, from which we can extract the total number in the distribution N and the number in the Thomas-Fermi part N_{TF}. The Thomas-Fermi fraction (A.3) is then

computed as $f_{\mathrm{TF}} = N_{\mathrm{TF}}/N - 0.054$, corrected for an experimentally determined fit offset. At low temperatures, the thermal distribution becomes comparable in size to the Thomas-Fermi part, causing the fit to underestimate f_{TF}. Both lattice depths show the emergence of a Thomas-Fermi fraction in $n(p_{\|})$ near 200 nK. This corresponds to a coherent part and finite in-plane phase stiffness. We identify this as the onset of the BKT transition in isolated pancakes. We expect little difference in the BKT transition temperature between the two lattice depths; the band gap and the compression of the planes scale weakly with lattice depth in our relatively shallow lattices.

At lower temperatures coherence between planes emerges in the form of interference effects in $n_{\perp}(p)$. Identically prepared clouds look radically different from one another in TOF (see A.4 for example images). The average of images at the same conditions is featureless, as shown in A.5, so useful information is contained in the fluctuations. Inspired by Fang et al.'s success in identifying phases of matter in 1D Bose gases [97], which exhibit strong phase fluctuations, we apply a similar analysis to our data. We normalize our distributions to $\sum_p n_{\perp}(p) = 1$, sort them into 25 nK bins and calculate the average distributions $\overline{n}_{\perp}(p,T)$. We then calculate the deviation of each cloud from the average for its bin, $\delta n_{\perp,i}(p,T) = n_{\perp,i}(p,T) - \overline{n}_{\perp}(p,T)$, and calculate the two-body fluctuation correlation function $\alpha_i(p_a,p_b,T) = \delta n_{\perp,i}(p_a,T)\delta n_{\perp,i}(p_b,T)$. The averages of those quantities, $\overline{\alpha}(p_a,p_b,T)$, are displayed in A.6. Along a line from lower left to upper right is the fluctuation power spectrum $\overline{\alpha}(p,p,T)$. From upper left to lower right is the opposite-momentum power spectrum $\overline{\alpha}(p,-p,T)$. A.7 normalizes the latter by the former, and is a measure of fractional correlations of opposite momenta, $\beta = 2\overline{\alpha}(p,-p,T)/[\overline{\alpha}(p,p,T)+\overline{\alpha}(-p,-p,T)]$. Together these show qualitative changes as a function of temperature and

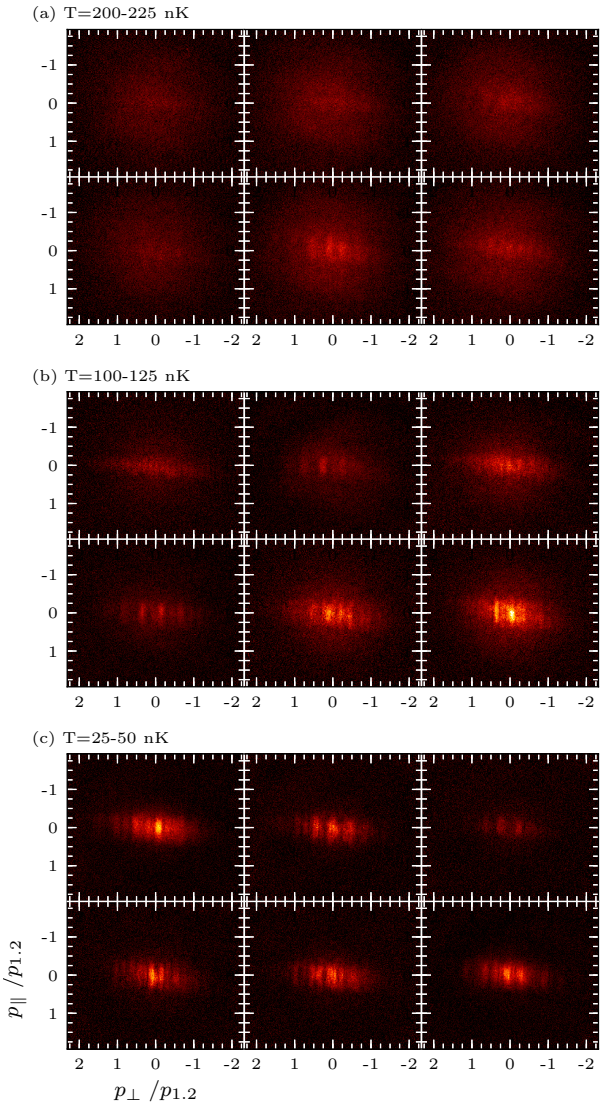

Figure A.4: A random sampling of images at a few temperature ranges in our 2.8 kHz lattice. Top: 200 nK–225 nK; middle: 100 nK–125 nK; bottom: 25 nK–50 nK.

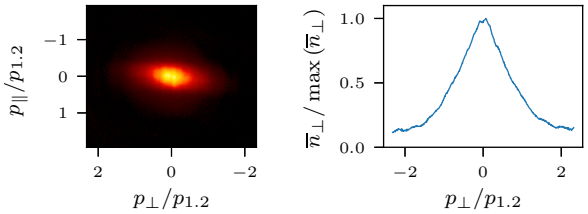

Figure A.5: The (left) average density profile for shots in the 2.8 kHz potential with temperatures between 25 nK and 50 nK, and (right) $\overline{n}_\perp$ for the same conditions. Neither shows any structure, despite the wide variation seen in A.4.

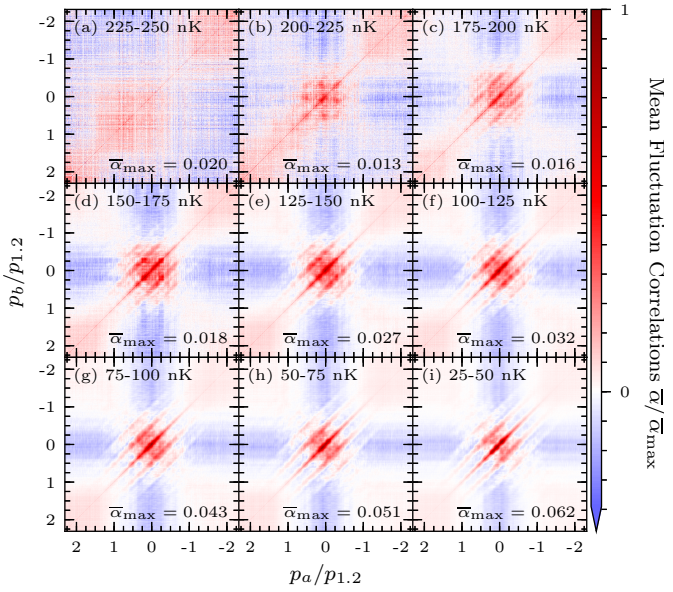

Figure A.6: We display the mean fluctuation correlations of the momentum, $\overline{\alpha}(p_a, p_b, T)$, at decreasing temperatures in panels (a)–(i), with the color scale in each panel normalized to the maximum $\overline{\alpha}_{\max}$. The features at the edge of the panels are artifacts of our normalization scheme. The temperature bins are 25 nK wide, and range monotonically from 225 nK–250 nK in panel (a) to 25 nK–50 nK in panel (i). Note the emergence of distinct momentum peaks in opposite momenta, which do not correspond to the sublattice recoil momenta. The longest length scale resolved is 10.9 µm.

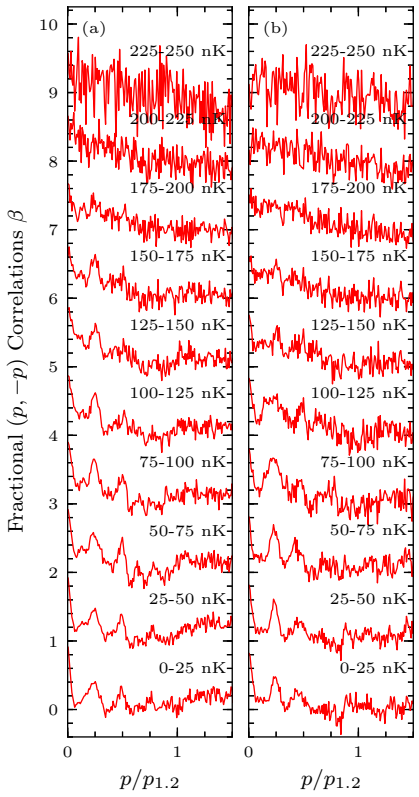

Figure A.7: Normalized $p,-p$ correlations $\beta = 2\overline{\alpha}(p,-p,T)/[\overline{\alpha}(p,p,T)+\overline{\alpha}(-p,-p,T)]$ for (a) the 2.8 kHz and (b) the deeper 5.6 kHz lattice. Thermal correlations persist to lower temperatures in (b) than (a), despite similar coherent fraction as seen in A.3.

lattice depth. In concert with our measurement of in-plane coherent fraction, we identify those differences with a set of phases of matter.

Our atomic gases are finite in size and harmonically trapped in all three dimensions. While disorder plays a strong role in the onset of superfluidity in each pancake, our harmonic trap favors emergence of order from its center. Consequently there are likely multiple phases of matter in most of our temperature bins. The 2.8 kHz lattice exhibits several competing varieties of correlation in $\overline{\alpha}$ as a function of temperature. Isotropic thermal correlations dominate along the lattice between 250 nK and 175 nK as seen in A.6(a)–(c), when the coherent fraction in plane is insufficient to give rise to interference effects. The lack of any structure in the normalized correlations β is apparent in A.7(a). The apparent

nonzero correlations in the thermal state derive from the finite width of the temperature bins. Colder clouds have smaller rms widths, and vice versa, so fluctuation amplitudes are symmetric about $p_\perp = 0$ and nonzero. The thermal nature of the correlations imply that $\rho_s^\perp = 0$. Below 200 nK, we begin to see the growth of a coherent fraction in A.3, implying that $\rho_s^\parallel > 0$. Concurrent $\rho_s^\perp = 0$ and $\rho_s^\parallel > 0$ constitute evidence of a sliding phase, a phase exhibiting 2D superfluidity in a 3D bulk, consistent with an anomalous Griffiths phase [32, 85, 86].

Correlations in our 2.8 kHz lattice begin to exhibit structure below 175 nK as seen in A.6(d). We use a multi peak Gaussian fit as a generic localized distribution to analyze our β distributions. Strong positive correlations in $(p_\perp,-p_\perp)$ emerge around $p_\perp = 0$, and momenta corresponding near wavelengths of 2.4 µm, 3.0 µm, 4.9 µm and 10.8 µm. The 4.9 µm and 10.8 µm modes blend together into one broad peak at temperatures below 50 nK, as do those at 2.4 µm and 3.0 µm, and at our lowest temperatures 3.0 µm correlations are suppressed. These emergent length scales are distinct from the periods composing our disordered potential (1.21 µm, 1.37 µm, 1.58 µm, 2.02 µm, 2.50 µm, 2.79 µm and 4.70 µm). Both the momenta peaks in the correlation spectra and the lattice recoil momenta were measured with the same optical system, thus there is no scale-factor uncertainty between the two. There is a peak in β nearby the 2.50 µm lattice. However, there is nothing special in our potential about this component, for it is neither the shortest nor the longest period in the potential, and its amplitude and phase are chosen in the same manner as every other component. The correlations on the 4.9 µm and 10.8 µm length scales are larger than any imposed by our disorder. We do not see any peaks in $\overline{\alpha}$ corresponding to the recoil momenta of the four lattices with the smallest periods.

While correlation peaks may emerge in completely incoherent lattice systems due to uncorrelated phase noise [98, 99], this does not explain our results. We confirmed this with a simple 1D single-particle simulation of noninteracting thermal distributions in our disordered lattice, which did not match our results. The simulations show correlations at low temperature, which depend on choice of relative phases, exist for each sub-lattice below 50 nK, and emerge first in high momentum states. In contrast, experimentally observed correlation peaks are evident at higher temperatures ($\approx$ 175 nK), only occur at a few momenta, and emerge first at low momentum.

The length scales of fluctuations depend on two factors. First, the lattice imposes structure on the coherent fraction; second, the temperature determines the size of coherently connected lattice sites ("puddles") and the distances between them. As the temperature is lowered, the system transitions to a fully connected puddle and lowering the temperature further has no effect. We attribute this transition to the population of many-body phonon modes as more pancakes undergo the BKT transition, leading to larger superfluid puddles and increasing overall coherent fraction. This is the process described by [85], as the anomalous Griffiths phase proceeds towards the superfluid transition with decreasing temperature.

This structure first emerges as peaks in A.6(d), and then settles to its final forms in A.7(a) below 100 nK. As mentioned, we interpret the settled form of β below 100 nK as the establishment of complete connectivity. This suggests that below 100 nK the system has crossed over to a Griffiths superfluid phase from an anomalous Griffiths phase. While we cannot measure phase stiffness directly, we expect it to be quite small in this regime [32, 85].

The same trend can be seen in the 5.6 kHz lattice data in A.7(b), but at much lower

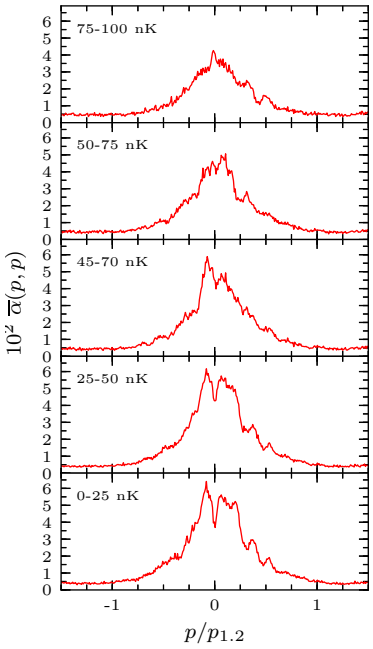

Figure A.8: Displayed are the square fluctuations $\overline{\alpha}(p,p)$ for a few choices of temperature in our 2.8 kHz lattice. A drop in fluctuations at $p = 0$ emerges below 70($\pm$2.5)nK.

temperatures, despite the coherent fraction's concurrent growth with the 2.8 kHz lattice. The disordered lattice in this data set is twice as deep, so we would expect the most depleted pancake's phase-space density, and thus transition temperature, to drop by $1/e$, and we see no evidence it ever leaves the sliding phase.

At temperatures below 70 nK, in our 2.8 kHz lattice, we observe a drop in the fluctuation power spectrum $\overline{\alpha}(p,p)$ at $p = 0$, as shown in A.8. Its contrast increases with decreasing temperature. We take this as evidence of the suppression of fluctuations due to Bose statistics of a macroscopically occupied, nonlocal state. This is consistent with the onset of finite phase stiffness along the disorder. We find it difficult to draw a clear line between a superfluid Griffiths phase and a full 3D superfluid. The literature does not discriminate between the two phases using parameters accessible with our system [85, 86], and Ref. [32] does not identify a distinction. If there are two such distinct phases, this macroscopically

ordered region is likely the latter.

A.5 Conclusion

Using our HiBAL we engineered an optical field isotropic in two dimensions and disordered in the third dimension. We explored the phase diagram of a previously unrealized class of disordered system. The momentum distributions of individual realizations vary wildly, thus we examined noise correlations as our experimental measure. Although we cannot directly measure phase stiffness (the primary parameter calculated theoretically), we observe trends with temperature consistent with the predictions of this Griffiths system. At high temperatures, distributions show no coherent (low momentum) features in plane and no correlations out of plane. As the temperature lowers, a low momentum (Thomas-Fermi-like) feature appears in plane, suggesting superfluidity in plane, while the out-of-plane correlations are still absent. At even lower temperatures, coherence between planes becomes apparent as a $p_\perp = 0$ peak in the out-of-plane correlations appears along with correlation features at nonzero momenta. Notably we observe discrete momentum peaks in the correlations unrelated to the momentum components of the disordered lattice. This suggests local correlations as some regions within the disordered potential become phase coherent, which is characteristic of the anomalous Griffiths phase. Finally, below 100 nK the noise correlations change little, suggesting full three-dimensional superfluidity (or at least coherence), although the correlation function is still quite different than a superfluid in a lattice without disorder. At a deeper lattice potential, similar phenomena are observed although the onsets are at lower temperatures, as might be expected as the disorder is

better able to prevent coherence buildup. Direct comparison with theory is needed to fully understand this disordered system, and given experimental limitations, would require calculations beyond phase stiffness.

Our HiBAL is a flexible platform capable of generating arbitrary sets of optical lattices over two spatial octaves with phase, amplitude, and wave-vector control at MHz frequencies. It will enable a large set of experiments, from transport measurements in disordered systems and the production of Hamiltonians for the study of Floquet physics, simultaneous with Bragg spectroscopy of all of the above.

Acknowledgements

We would like to thank I. Spielman for the extensive discussions during the preparation of this manuscript.

Appendix B: Commutation relations for $\mathcal{D}_\kappa$ and $\mathcal{Y}_\alpha$

These follow from the canonical commutation relations for x, p and the definitions of $\mathcal{D}_\kappa$ and $\mathcal{Y}_\alpha$

For $\mathcal{D}_\kappa$,

$$\mathcal{D}_\kappa x \mathcal{D}_\kappa^\dagger = \kappa x \tag{B.1}$$

$$\mathcal{D}_\kappa p \mathcal{D}_\kappa^\dagger = \frac{p}{\kappa} \tag{B.2}$$

$$\dot{\mathcal{D}}_\kappa \mathcal{D}_\kappa^\dagger = \frac{i\dot{\kappa}}{\hbar\kappa} \frac{xp + px}{2}. \tag{B.3}$$

And for $\mathcal{Y}_\alpha$,

$$\mathcal{Y}_\alpha x \mathcal{Y}_\alpha^\dagger = x \tag{B.4}$$

$$\mathcal{Y}_\alpha p \mathcal{Y}_\alpha^\dagger = (p + \alpha x) \tag{B.5}$$

$$\dot{\mathcal{Y}}_\alpha \mathcal{Y}_\alpha^\dagger = -\frac{i}{\hbar} \frac{\dot{\alpha} x^2}{2} \tag{B.6}$$

Appendix C: Proof of Floquet's Theorem

We follow [100] in our presentation of the proof.

As stated in chapter 4, for a problem of the form

$$\mathbf{x}' = \mathbf{A}(t)\mathbf{x} \tag{C.1}$$

where $\mathbf{A}(t)$ is periodic with a period T. Floquet's theorem then states that for all solutions $\mathbf{x}$ the following are true:

1. $\mathbf{x}$ may not necessarily be periodic, but it must be of the form $e^{\mu t}\mathbf{p}(t)$, where $\mathbf{p}(t)$ is T periodic.

2. There exist n such μ_j, and they satisfy the condition:

$$e^{\mu_1 T}e^{\mu_2 T}\cdots e^{\mu_n T} = \exp\left(\int_0^T \operatorname{tr}\mathbf{A}(q)dq\right) \tag{C.2}$$

We will first prove some lemmas that will help us in proving this result.

Definition C.0.1. (Fundamental Matrix) Let $\mathbf{x}^1(t), \cdots, \mathbf{x}^n(t)$ be n solutions of $\mathbf{x}' = \mathbf{A}(t)\mathbf{x}$, and let

$$\mathbf{X}(t) = \left[\left[\mathbf{x^1}\right]\cdots\left[\mathbf{x^n}\right]\right] \tag{C.3}$$

such that $\mathbf{X}(t)$ is an $n \times n$ solutions of $\mathbf{X}' = \mathbf{AX}$. If all $\mathbf{x^n}(t)$ are linearly independent, then $\mathbf{X}(t)$ is non-singular and is often called a fundamental matrix If $\mathbf{X}(t_0) = \mathbf{I}$, then $\mathbf{X}$ is the principal fundamental matrix

Lemma C.0.1. If $\mathbf{X(t)}$ is a fundamental matrix then so is $\mathbf{Y(t)} = \mathbf{X}(t)\mathbf{B}$ for any non-singular constant matrix $\mathbf{B}$

Proof. Since $\mathbf{X}(t)$ and $\mathbf{B}$ are non-singular then so is $\mathbf{Y}^{-1} = \mathbf{B}^{-1}\mathbf{X}^{-1}(t)$ and hence $\mathbf{Y}(t)$ is also non-singular. And,

$$\mathbf{Y}' = \mathbf{X}'\mathbf{B} = \mathbf{AXB} = \mathbf{AY} \tag{C.4}$$

□

Lemma C.0.2. Let the Wronskian W(t) of $\mathbf{X}(t)$ be the determinant of $\mathbf{X}(t)$. Then

$$W(t) = W(t_0) \exp\left(\int_{t_0}^{t} tr(\mathbf{A}(q))dq\right) \tag{C.5}$$

Proof. Let t_0 be some time. Expand $\mathbf{X}(t)$ in a Taylor series:

$$\mathbf{X}(t) = \mathbf{X}(t_0) + (t - t_0)\mathbf{X}'(t_0) + \mathcal{O}\left((t - t_0)^2\right) \tag{C.6}$$

$$= \mathbf{X}(t_0) + (t - t_0)\mathbf{A}(t_0)\mathbf{X}(t_0) + \mathcal{O}\left((t - t_0)^2\right) \tag{C.7}$$

$$= [\mathbf{I} + (t - t_0)\mathbf{A}(t_0)]\mathbf{X}(t_0) + \mathcal{O}\left((t - t_0)^2\right) \tag{C.8}$$

this implies that

$$\det(\mathbf{X(t)}) = \det[\mathbf{I} + (t - t_0)\mathbf{A}(t_0)] \det[\mathbf{X}(t_0)] \tag{C.9}$$

$$W(t) = \det[\mathbf{I} + (t - t_0)\mathbf{A}(t_0)]W(t_0). \tag{C.10}$$

If we now expand $W(t)$ in a Taylor series,

$$W(t) = W(t_0) + (t - t_0)W'(t_0) + \mathcal{O}\left((t - t_0)^2\right) \tag{C.11}$$

and use the fact that

$$\det(\mathbf{I} + \epsilon\mathbf{C}) = 1 + \epsilon \operatorname{tr}(\mathbf{C}) + \mathcal{O}\left(\epsilon^2\right). \tag{C.12}$$

We can infer that

$$W'(t_0) = W(t_0) \operatorname{tr}(\mathbf{A}(t_0)) \tag{C.13}$$

Since t_0 is arbitrary, this is equivalent to

$$W'(t) = W(t) \operatorname{tr}(\mathbf{A}(t)). \tag{C.14}$$

This is a simple differential equation, and is solved by

$$W(t) = W(t_0) \exp\left(\int_{t_0}^{t} \operatorname{tr}(\mathbf{A}(q)dq\right) \tag{C.15}$$

□

Theorem C.0.3. Let $\mathbf{A}(t)$ be a T-periodic matrix. If $\mathbf{X}(t)$ is a fundamental matrix then so is $\mathbf{X}(t + T)$ and there exists a non-singular constant matrix $\mathbf{B}$ such that

1. $\mathbf{X}(t + T) = \mathbf{X}(t)\mathbf{B}$ for all t
2. $\det(\mathbf{B}) = \exp\left(\int_0^T \operatorname{tr}(\mathbf{A}(q))dq\right)$

Proof. Consider $\mathbf{Y}(t) = \mathbf{X}(t+T)$, we will show that $\mathbf{Y}(t)$ is also a fundamental matrix.

$$\mathbf{Y}'(t) = \mathbf{X}'(t+T) = \mathbf{A}(t+T)\mathbf{X}(t+T) = \mathbf{A}(t)\mathbf{Y}(t) \tag{C.16}$$

Hence, $\mathbf{X}(t+T)$ is also a fundamental matrix. Now,

1. Let $\mathbf{B}(t) = \mathbf{X}^{-1}(t)\mathbf{Y}(t)$. Then,

$$\mathbf{Y}(t) = \mathbf{X}(t)\mathbf{X}^{-1}(t)\mathbf{Y}(t) \tag{C.17}$$

$$= \mathbf{X}(t)\mathbf{B}(t) \tag{C.18}$$

   If we let $\mathbf{B}_0 = \mathbf{B}(t_0)$. Then we know by Lemma C.0.1 that $\mathbf{Y}_0(t) = \mathbf{X}(t)\mathbf{B}_0$ is a fundamental matrix. And since both $\mathbf{Y}_0(t)$ and $\mathbf{Y}(t)$ are solutions to the same equation, uniqueness of solutions demands that they be equal. Hence we have $\mathbf{Y}_0(t) = \mathbf{Y}(t)$ for all t. Therefore, $\mathbf{B}_0 = \mathbf{B}(t)$ and $\mathbf{B}$ is time independent.

2. From Lemma C.0.2, we know that

$$W(t) = W(t_0)\exp\left(\int_{t_0}^{t} \operatorname{tr}(\mathbf{A}(q))dq\right) \tag{C.19}$$

$$W(t+T) = W(t_0)\exp\left(\int_{t_0}^{t} \operatorname{tr}(\mathbf{A}(q))dq + \int_{t}^{t+T} (\mathbf{A}(q))dq\right) \tag{C.20}$$

$$W(t+T) = W(t)\exp\left(\int_{t}^{t+T} (\mathbf{A}(q))dq\right) \tag{C.21}$$

$$W(t+T) = W(t)\exp\left(\int_{0}^{T} (\mathbf{A}(q))dq\right). \tag{C.22}$$

$$\tag{C.23}$$

and,

$$\mathbf{X}(t+T) = \mathbf{X}(t)\mathbf{B} \tag{C.24}$$

$$\det(\mathbf{X}(t+T)) = \det(\mathbf{X}(t))\det(\mathbf{B}) \tag{C.25}$$

$$W(t+T) = W(t)\det(\mathbf{B}). \tag{C.26}$$

Together, these imply that

$$\det(\mathbf{B}) = \exp\left(\int_0^T (\mathbf{A}(q))dq\right) \tag{C.27}$$

□

These result allows to compute $\mathbf{B}$ by choosing a time t. In particular, for $t = 0$, $\mathbf{B} = \mathbf{X}^{-1}(0)\mathbf{X}(T)$. If we set our initial condition as $\mathbf{X}(0) = \mathbf{I}$, then $\mathbf{B} = \mathbf{X}(T)$.[1]

Before proving the main result, we need one more definition.

Definition C.0.2. (Characteristic Multipliers and Exponents) The eigenvalues $\rho_1, \ldots, \rho_n$ of $\mathbf{B}$ are called the characteristic multipliers for $\mathbf{X}'(t) = \mathbf{A}(t)\mathbf{X}(t)$. The characteristic exponents or the Floquet exponents are $\mu_1, \ldots, \mu_n$ satisfying

$$\rho_1 = e^{\mu_1 T}, \quad \rho_2 = e^{\mu_2 T}, \quad \ldots, \quad \rho_n = e^{\mu_n T} \tag{C.28}$$

μ_j for $j \in N$ could in general be complex. Things to note,

[1] If we think in terms of Quantum mechanics, this allows us to write the time-independent Floquet hamiltonian, $\mathcal{H}$ in terms of the time-dependent hamiltonian H

1. The characteristic multipliers $\rho_1, \ldots, \rho_n$ of $\mathbf{B} = \mathbf{X}(T)$ obey the condition

$$\det(\mathbf{B}) = \rho_1 \rho_2 \ldots \rho_n = \exp\left(\int_0^T \operatorname{tr}(\mathbf{A}(s))ds\right) \tag{C.29}$$

   for $\mathbf{X}(\mathbf{0}) = \mathbf{I}$. This follows from the previous theorem

2. The characteristic exponents are not unique, as $e^{\rho_j T} = e^{(\rho_j + 2\pi i/T)T}$

3. The ρ_j are a property of the equation $\mathbf{X}'(t) = \mathbf{A}\mathbf{X}$ and do not depend on the particular fundamental matrix chosen.

   Proof. Take $\mathbf{X}'(t)$ to be another fundamental matrix. Then by Theorem C.0.3

$$\mathbf{X}'(t) = \mathbf{X}(t)\mathbf{B}' \tag{C.30}$$

   We showed earlier that for two fundamental matrices $\mathbf{X}$ and $\mathbf{X}'$, there is a constant non-singular matrix $\mathbf{C}$ such that

$$\mathbf{X}'(t) = \mathbf{X}(t)\mathbf{C} \tag{C.31}$$

now,

$$(\mathbf{X}'(t)\mathbf{B}') = (\mathbf{X}(t)\mathbf{B})\,\mathbf{C} \tag{C.32}$$

$$\mathbf{X}(t)\mathbf{C}\mathbf{B}' = \mathbf{X}(t)\mathbf{B}\mathbf{C} \tag{C.33}$$

$$\mathbf{C}\mathbf{B}' = \mathbf{B}\mathbf{C} \tag{C.34}$$

$$\mathbf{C}\mathbf{B}'\mathbf{C}^{-1} = \mathbf{B} \tag{C.35}$$

So the eigenvalues of $\mathbf{B}'$ and $\mathbf{B}$ are the same, therefore the ρ_j are also the same. □

Theorem C.0.4. For a given characteristic multiplierρ and its corresponding exponent μ ($\rho = e^{\mu T}$), there exists a solution $\mathbf{x}(t)$ of $\mathbf{x}' = \mathbf{A}(t)\mathbf{x}$ such that

1. $\mathbf{x}(t+T) = \rho\mathbf{x}(t)$
2. A periodic solution, $\mathbf{p}(t)$, with the period T exists, and $\mathbf{x}(t) = e^{\mu t}\mathbf{p}(t)$

Proof. 1. Take the eigenvector $\mathbf{b}$ of $\mathbf{B}$ with eigenvalue ρ. Let $\mathbf{x}(t) = \mathbf{X}(t)\mathbf{b}$. Now, $\mathbf{x}' = \mathbf{A}\mathbf{x}$ and

$$\begin{aligned}\mathbf{x}(t+T) &= \mathbf{X}(t+T)\mathbf{b}\\ &= \mathbf{X}(t)\mathbf{B}\mathbf{b}\\ &= \rho\mathbf{X}(t)\mathbf{b}\\ &= \rho\mathbf{x}(t)\end{aligned} \tag{C.36}$$

2. Let $\mathbf{p}(t) = \mathbf{x}(t)e^{-\mu t}$, now

$$\begin{aligned}
\mathbf{p}(t+T) &= \mathbf{x}(t+T)e^{-\mu(t+T)} \\
&= \rho\mathbf{x}(t)e^{-\mu(t+T)} \\
&= (\rho e^{-\mu T})\mathbf{x}(t)e^{-\mu t} \\
&= \mathbf{x}(t)e^{-\mu t} \\
&= \mathbf{p}(t)
\end{aligned} \tag{C.37}$$

□

This proves all the claims made in the original statement of Floquet's theorem.

Bibliography

[1] Zachary Smith. Bose Einstein Condensates in Dynamically Controlled Optical Lattices. 2019.

[2] Bose. Plancks gesetz und lichtquantenhypothese. Zeitschrift für Physik, 26:178–181, 1924.

[3] M. H. Anderson, J. R. Ensher, M. R. Matthews, C. E. Wieman, and E. A. Cornell. Observation of bose-einstein condensation in a dilute atomic vapor. Science, 269(5221):198–201, 1995.

[4] K. B. Davis, M. O. Mewes, M. R. Andrews, N. J. van Druten, D. S. Durfee, D. M. Kurn, and W. Ketterle. Bose-einstein condensation in a gas of sodium atoms. Phys. Rev. Lett., 75:3969–3973, Nov 1995.

[5] C. Gross, T. Zibold, E. Nicklas, J. Estève, and M. K. Oberthaler. Nonlinear atom interferometer surpasses classical precision limit. Nature, 464(7292):1165–1169, April 2010.

[6] Ch Salomon, N. Dimarcq, M. Abgrall, A. Clairon, P. Laurent, P. Lemonde, G. Santarelli, P. Uhrich, L. G. Bernier, G. Busca, A. Jornod, P. Thomann, E. Samain, P. Wolf, F. Gonzalez, Ph Guillemot, S. Leon, F. Nouel, Ch Sirmain, and S. Feltham. Cold atoms in space and atomic clocks: ACES. Comptes Rendus de l'Académie des Sciences - Series IV - Physics, 2(9):1313–1330, 2001.

[7] Tupac Bravo, Carlos Sabín, and Ivette Fuentes. Analog quantum simulation of gravitational waves in a Bose-Einstein condensate. EPJ Quantum Technology, 2(1):3, January 2015.

[8] J. Bardeen, L. N. Cooper, and J. R. Schrieffer. Microscopic theory of superconductivity. Phys. Rev., 106:162–164, Apr 1957.

[9] Christopher Pethick and Henrik Smith. Bose-Einstein condensation in dilute gases. Cambridge University Press, Cambridge ; New York, 2nd ed edition, 2008.

[10] Christopher J Foot. Atomic physics. Oxford master series in atomic, optical, and laser physics. Oxford University Press, Oxford, 2007.

[11] H.J. Metcalf and Peter van der Straten. Laser cooling and trapping. Journal of the Optical Society of America B, 20, 05 2003.

[12] S Stenholm. Laser cooling and trapping. European Journal of Physics, 9(4):242, oct 1988.

[13] J. Dalibard and C. Cohen-Tannoudji. Laser cooling below the doppler limit by polarization gradients: simple theoretical models. J. Opt. Soc. Am. B, 6(11):2023–2045, Nov 1989.

[14] Steven Chu, L. Hollberg, J. E. Bjorkholm, Alex Cable, and A. Ashkin. Three-dimensional viscous confinement and cooling of atoms by resonance radiation pressure. Phys. Rev. Lett., 55:48–51, Jul 1985.

[15] William D. Phillips and Harold Metcalf. Laser deceleration of an atomic beam. Phys. Rev. Lett., 48:596–599, Mar 1982.

[16] E. L. Raab, M. Prentiss, Alex Cable, Steven Chu, and D. E. Pritchard. Trapping of neutral sodium atoms with radiation pressure. Phys. Rev. Lett., 59:2631–2634, Dec 1987.

[17] Alan L. Migdall, John V. Prodan, William D. Phillips, Thomas H. Bergeman, and Harold J. Metcalf. First observation of magnetically trapped neutral atoms. Phys. Rev. Lett., 54:2596–2599, Jun 1985.

[18] D. M. Harber, J. M. McGuirk, J. M. Obrecht, and E. A. Cornell. Thermally Induced Losses in Ultra-Cold Atoms Magnetically Trapped Near Room-Temperature Surfaces. Journal of Low Temperature Physics, 133(3):229–238, November 2003.

[19] William D. Phillips and Harold Metcalf. Laser deceleration of an atomic beam. Phys. Rev. Lett., 48:596–599, Mar 1982.

[20] M. D. Barrett, J. A. Sauer, and M. S. Chapman. All-optical formation of an atomic bose-einstein condensate. Phys. Rev. Lett., 87:010404, Jun 2001.

[21] J. Dalibard and C. Cohen-Tannoudji. Laser cooling below the doppler limit by polarization gradients: simple theoretical models. J. Opt. Soc. Am. B, 6(11):2023–2045, Nov 1989.

[22] Paul D. Lett, Richard N. Watts, Christoph I. Westbrook, William D. Phillips, Phillip L. Gould, and Harold J. Metcalf. Observation of atoms laser cooled below the doppler limit. Phys. Rev. Lett., 61:169–172, Jul 1988.

[23] E. L. Surkov, J. T. M. Walraven, and G. V. Shlyapnikov. Collisionless motion and evaporative cooling of atoms in magnetic traps. Phys. Rev. A, 53:3403–3408, May 1996.

[24] I. D. Setija, H. G. C. Werij, O. J. Luiten, M. W. Reynolds, T. W. Hijmans, and J. T. M. Walraven. Optical cooling of atomic hydrogen in a magnetic trap. Phys. Rev. Lett., 70:2257–2260, Apr 1993.

[25] Toshiya Kinoshita, Trevor Wenger, and David S. Weiss. All-optical bose-einstein condensation using a compressible crossed dipole trap. Phys. Rev. A, 71:011602, Jan 2005.

[26] Abraham J. Olson, Robert J. Niffenegger, and Yong P. Chen. Optimizing the efficiency of evaporative cooling in optical dipole traps. Phys. Rev. A, 87:053613, May 2013.

[27] Wolfgang Ketterle and N. J. van Druten. Bose-einstein condensation of a finite number of particles trapped in one or three dimensions. Phys. Rev. A, 54:656–660, Jul 1996.

[28] Daniel Steck. Rubidium 87 d line data. page 0, 01 2023.

[29] Miroslav Gajdacz, Poul Pedersen, Troels Mørch, Andrew Hilliard, Jan Arlt, and Jacob Sherson. Non-destructive Faraday imaging of dynamically controlled ultracold atoms. In APS Division of Atomic, Molecular and Optical Physics Meeting Abstracts, volume 2013 of APS Meeting Abstracts, page M1.004, May 2013.

[30] J. E. Lye, J. J. Hope, and J. D. Close. Nondestructive dynamic detectors for bose-einstein condensates. Phys. Rev. A, 67:043609, Apr 2003.

[31] Beer. Bestimmung der absorption des rothen lichts in farbigen flüssigkeiten. Annalen der Physik, 162(5):78–88, 1852.

[32] Nicolas Laflorencie. Sliding phase in randomly stacked 2d superfluids/superconductors. 99(6):66001.

[33] Matthew Earl Wallace Reed. An Experimental Realization of a Griffiths Phase in 87Rb in Three Dimensions. 2017.

[34] Y.-J. Lin, A. R. Perry, R. L. Compton, I. B. Spielman, and J. V. Porto. Rapid production of ^{87}Rb bose-einstein condensates in a combined magnetic and optical potential. Phys. Rev. A, 79:063631, Jun 2009.

[35] Matthew Charles Beeler. Disordered Ultracold Two-Dimensional Bose Gases. 2011.

[36] Colin V. Parker, Li-Chung Ha, and Cheng Chin. Direct observation of effective ferromagnetic domains of cold atoms in a shaken optical lattice. Nature Physics, 9(12):769–774, December 2013.

[37] Sayan Choudhury and Erich J. Mueller. Stability of a floquet bose-einstein condensate in a one-dimensional optical lattice. Phys. Rev. A, 90:013621, Jul 2014.

[38] G. Floquet. Sur les équations différentielles linéaires à coefficients périodiques. Annales scientifiques de l'École Normale Supérieure, 12:47–88, 1883.

[39] Jon H. Shirley. Solution of the Schrödinger Equation with a Hamiltonian Periodic in Time. Phys. Rev., 138(4B):B979–B987, May 1965.

[40] Konrad Viebahn. Introduction to Floquet theory.

[41] Mark S. Rudner and Netanel H. Lindner. The floquet engineer's handbook, 2020.

[42] A. Gómez-León and G. Platero. Floquet-bloch theory and topology in periodically driven lattices. Phys. Rev. Lett., 110:200403, May 2013.

[43] Logan W. Clark, Brandon M. Anderson, Lei Feng, Anita Gaj, K. Levin, and Cheng Chin. Observation of density-dependent gauge fields in a bose-einstein condensate based on micromotion control in a shaken two-dimensional lattice. Phys. Rev. Lett., 121:030402, Jul 2018.

[44] Li-Chung Ha, Logan W. Clark, Colin V. Parker, Brandon M. Anderson, and Cheng Chin. Roton-maxon excitation spectrum of bose condensates in a shaken optical lattice. Phys. Rev. Lett., 114:055301, Feb 2015.

[45] Wei Zheng, Boyang Liu, Jiao Miao, Cheng Chin, and Hui Zhai. Strong interaction effects and criticality of bosons in shaken optical lattices. Phys. Rev. Lett., 113:155303, Oct 2014.

[46] H. Lignier, C. Sias, D. Ciampini, Y. Singh, A. Zenesini, O. Morsch, and E. Arimondo. Dynamical control of matter-wave tunneling in periodic potentials. Phys. Rev. Lett., 99:220403, Nov 2007.

[47] André Eckardt, Christoph Weiss, and Martin Holthaus. Superfluid-insulator transition in a periodically driven optical lattice. Phys. Rev. Lett., 95:260404, Dec 2005.

[48] C. A. Weidner and Dana Z. Anderson. Experimental demonstration of shaken-lattice interferometry. Phys. Rev. Lett., 120:263201, Jun 2018.

[49] J. L. Ville, T. Bienaimé, R. Saint-Jalm, L. Corman, M. Aidelsburger, L. Chomaz, K. Kleinlein, D. Perconte, S. Nascimbène, J. Dalibard, and J. Beugnon. Loading and compression of a single two-dimensional bose gas in an optical accordion. Phys. Rev. A, 95:013632, Jan 2017.

[50] R. A. Williams, J. D. Pillet, S. Al-Assam, B. Fletcher, M. Shotter, and C. J. Foot. Dynamic optical lattices: two-dimensional rotating and accordion lattices for ultracold atoms. Optics Express, 16(21):16977, October 2008.

[51] T. C. Li, H. Kelkar, D. Medellin, and M. G. Raizen. Real-time control of the periodicity of a standing wave: an optical accordion. Opt. Express, 16(8):5465–5470, Apr 2008.

[52] Leonardo Fallani, Chiara Fort, Jessica E. Lye, and Massimo Inguscio. Bose-einstein condensate in an optical lattice with tunable spacing: transport and static properties. Optics Express, 13(11):4303, 2005.

[53] Neil W. Ashcroft and N. David Mermin. Solid state physics. Holt, Rinehart and Winston, New York, 1976. tex.ids= ashcroft1976b.

[54] Charles Kittel. Introduction to Solid State Physics. Wiley, 8 edition, 2004.

[55] Felix Bloch. Über die Quantenmechanik der Elektronen in Kristallgittern. Zeitschrift für Physik, 52(7):555–600, July 1929.

[56] Émile Mathieu. Mémoire sur le mouvement vibratoire d'une membrane de forme elliptique. Journal de Mathématiques Pures et Appliquées, 13:137–203, 1868.

[57] Gregory H. Wannier. The structure of electronic excitation levels in insulating crystals. Phys. Rev., 52:191–197, Aug 1937.

[58] J. C. Slater and G. F. Koster. Simplified lcao method for the periodic potential problem. Phys. Rev., 94:1498–1524, Jun 1954.

[59] Python Core Team. Python: A dynamic, open source programming language. Python Software Foundation, 2019. Python version 3.7.

[60] Pauli Virtanen, Ralf Gommers, Travis E. Oliphant, Matt Haberland, Tyler Reddy, David Cournapeau, Evgeni Burovski, Pearu Peterson, Warren Weckesser, Jonathan Bright, Stéfan J. van der Walt, Matthew Brett, Joshua Wilson, K. Jarrod Millman, Nikolay Mayorov, Andrew R. J. Nelson, Eric Jones, Robert Kern, Eric Larson, CJ Carey, İlhan Polat, Yu Feng, Eric W. Moore, Jake VanderPlas, Denis Laxalde, Josef Perktold, Robert Cimrman, Ian Henriksen, E. A. Quintero, Charles R Harris, Anne M. Archibald, Antônio H. Ribeiro, Fabian Pedregosa, Paul van Mulbregt, and SciPy 1.0 Contributors. SciPy 1.0: Fundamental Algorithms for Scientific Computing in Python. Nature Methods, 2020.

[61] Charles R Harris, K Jarrod Millman, Stéfan J van der Walt, Ralf Gommers, Pauli Virtanen, David Cournapeau, Eric Wieser, Julian Taylor, Sebastian Berg, Nathaniel J Smith, Robert Kern, Matti Picus, Stephan Hoyer, Marten H van Kerkwijk, Matthew Brett, Allan Haldane, Jaime Fernández del Río, Mark Wiebe, Pearu Peterson, Pierre Gérard-Marchant, Kevin Sheppard, Tyler Reddy, Warren Weckesser, Hameer Abbasi, Christoph Gohlke, and Travis E Oliphant. Array programming with NumPy. Nature, 585(7825):357–362, 2020.

[62] Fredrik Johansson et al. mpmath: a Python library for arbitrary-precision floating-point arithmetic (version 0.14), February 2010. http://code.google.com/p/mpmath/.

[63] John D Hunter. Matplotlib: A 2d graphics environment. Computing in science & engineering, 9(3):90, 2007.

[64] Serge Aubry and Gilles André. Analyticity breaking and anderson localization in incommensurate lattices. Proceedings, VIII International Colloquium on Group-Theoretical Methods in Physics, 3, 01 1980.

[65] Giacomo Roati, Chiara D'Errico, Leonardo Fallani, Marco Fattori, Chiara Fort, Matteo Zaccanti, Giovanni Modugno, Michele Modugno, and Massimo Inguscio. Anderson localization of a non-interacting bose–einstein condensate. Nature, 453(7197):895–898, June 2008.

[66] Y. Lahini, R. Pugatch, F. Pozzi, M. Sorel, R. Morandotti, N. Davidson, and Y. Silberberg. Observation of a localization transition in quasiperiodic photonic lattices. Phys. Rev. Lett., 103:013901, Jun 2009.

[67] Tak-San Ho and Shih-I Chut. Semiclassical many-mode Floquet theory: 11. Nonlinear multiphoton dynamics of a two-level system in a strong bichromatic field.

[68] Tak-San Ho and Shih-I Chu. Semiclassical many-mode Floquet theory. IV. Coherent population trapping and SU(3) dynamical evolution of dissipative three-level systems in intense bichromatic fields. Phys. Rev. A, 32(1):377–395, July 1985.

[69] Tak-San Ho and Shih-I Chu. Semiclassical many-mode Floquet theory. III. SU(3) dynamical evolution of three-level systems in intense bichromatic fields. Phys. Rev. A, 31(2):659–676, February 1985.

[70] Wolfram Research, Inc. Mathematica, Version 14.0. Champaign, IL, 2024.

[71] Yuya Ikeda, Sota Kitamura, and Takahiro Morimoto. Floquet engineering of electric polarization with two-frequency drive. Progress of Theoretical and Experimental Physics, 2022(4):04A101, April 2022.

[72] Jin Hyoun Kang and Yong-il Shin. Topological Floquet engineering of a one-dimensional optical lattice via resonant shaking with two harmonic frequencies. Phys. Rev. A, 102(6):063315, December 2020.

[73] A. N. Poertner and J. D. D. Martin. On the validity of many-mode Floquet theory with commensurate frequencies. Phys. Rev. A, 101(3):032116, March 2020. arXiv:1912.02770 [physics, physics:quant-ph].

[74] Juliette Billy, Vincent Josse, Zhanchun Zuo, Alain Bernard, Ben Hambrecht, Pierre Lugan, David Clément, Laurent Sanchez-Palencia, Philippe Bouyer, and Alain Aspect. Direct observation of Anderson localization of matter waves in a controlled disorder. 453(7197):891–894.

[75] B. Allard, T. Plisson, M. Holzmann, G. Salomon, A. Aspect, P. Bouyer, and T. Bourdel. Effect of disorder close to the superfluid transition in a two-dimensional Bose gas. 85(3):033602.

[76] S. S. Kondov, W R McGehee, J J Zirbel, and B DeMarco. Three-Dimensional Anderson Localization of Ultracold Matter. 334(6052):66–68.

[77] M. C. Beeler, M E W Reed, T. Hong, and S. L. Rolston. Disorder-driven loss of phase coherence in a quasi-2D cold atom system. 14(7):073024.

[78] G. Semeghini, M. Landini, P. Castilho, S. Roy, G. Spagnolli, A. Trenkwalder, M. Fattori, M. Inguscio, and G. Modugno. Measurement of the mobility edge for 3D Anderson localization. 11(7):554–559.

[79] Carolyn Meldgin, Ushnish Ray, Philip Russ, David Chen, David M. Ceperley, and Brian DeMarco. Probing the Bose glass-superfluid transition using quantum quenches of disorder. 12(7):646–649.

[80] B. Deissler, M. Zaccanti, G. Roati, C. D'Errico, M. Fattori, M. Modugno, G. Modugno, and M. Inguscio. Delocalization of a disordered bosonic system by repulsive interactions. 6(5):354–358.

[81] E. E. Edwards, M. Beeler, Tao Hong, and S. L. Rolston. Adiabaticity and Localization in One-Dimensional Incommensurate Lattices. 101(26):260402.

[82] Michael Schreiber, Sean S. Hodgman, Pranjal Bordia, Henrik P. Lüschen, Mark H. Fischer, Ronen Vosk, Ehud Altman, Ulrich Schneider, and Immanuel Bloch. Observation of many-body localization of interacting fermions in a quasirandom optical lattice. 349(6250):842–845.

[83] Bryce Gadway, Daniel Pertot, Jeremy Reeves, Matthias Vogt, and Dominik Schneble. Glassy Behavior in a Binary Atomic Mixture. 107(14):145306.

[84] Z. Hadzibabic and J. Dalibard. Two-dimensional Bose fluids: An atomic physics perspective. 34(6):389–434.

[85] David Pekker, Gil Refael, and Eugene Demler. Finding the elusive sliding phase in the superfluid-normal phase transition smeared by c-axis disorder. 105(8):085302.

[86] Priyanka Mohan, Paul M. Goldbart, Rajesh Narayanan, John Toner, and Thomas Vojta. Anomalously Elastic Intermediate Phase in Randomly Layered Superfluids, Superconductors, and Planar Magnets. 105(8):085301.

[87] Thomas Vojta. Quantum Griffiths Effects and Smeared Phase Transitions in Metals: Theory and Experiment. 161(1-2):299–323.

[88] Mohit Randeria, James P. Sethna, and Richard G. Palmer. Low-Frequency Relaxation in Ising Spin-Glasses. 54(12):1321–1324.

[89] Robert B. Griffiths. Nonanalytic Behavior Above the Critical Point in a Random Ising Ferromagnet. 23(1):17–19.

[90] C. S. O'Hern, T. C. Lubensky, and J. Toner. Sliding Phases in XY Models, Crystals, and Cationic Lipid-DNA Complexes. 83(14):2745–2748.

[91] Sara Ubaid-Kassis, Thomas Vojta, and Almut Schroeder. Quantum griffiths phase in the weak itinerant ferromagnetic alloy Ni1-xVx. 104(6):066402.

[92] Ruizhe Wang, Adane Gebretsadik, Sara Ubaid-kassis, Almut Schroeder, Thomas Vojta, Peter J Baker, Francis L Pratt, Stephen J Blundell, Isabel Franke, S M Johannes, and Katharine Page. Supplemental material for Quantum Griffiths phase inside the ferromagnetic phase of Ni 1 - x V x. 118(26):10–12.

[93] Rémi Desbuquois, Lauriane Chomaz, Tarik Yefsah, Julian Léonard, Jérôme Beugnon, Christof Weitenberg, and Jean Dalibard. Superfluid behaviour of a two-dimensional Bose gas. 8(9):645–648.

[94] L. Mathey, A. Vishwanath, and E. Altman. Noise correlations in low-dimensional systems of ultracold atoms. 79(1):013609.

[95] Y.-J. Lin, A. R. Perry, R. L. Compton, I. B. Spielman, and J. V. Porto. Rapid production of ^{87}Rb bose-einstein condensates in a combined magnetic and optical potential. Phys. Rev. A, 79:063631, Jun 2009.

[96] Y. Castin and R. Dum. Bose-Einstein Condensates in Time Dependent Traps. 77(27):5315–5319.

[97] Bess Fang, Aisling Johnson, Tommaso Roscilde, and Isabelle Bouchoule. Momentum-Space Correlations of a One-Dimensional Bose Gas. 116(5):050402.

[98] S. Filling, Fabrice Gerbier, Artur Widera, Olaf Mandel, Tatjana Gericke, and Immanuel Bloch. Spatial quantum noise interferometry in expanding ultracold atom clouds. 2005:232–232.

[99] I. B. Spielman, W. D. Phillips, and J. V. Porto. Mott-insulator transition in a two-dimensional atomic bose gas. 98(8):080404.

[100] Michael J. Ward. Basic floquet theory.